THE EFFECTS OF LATTICE ANISOTROPIES ON THE PHYSICS OF COPPER OXIDE PLANES

J.M. Tipper

B.Sc. Physics, University of Lethbridge, 2001

A Thesis
Submitted to the School of Graduate Studies
of the University of Lethbridge
in Partial Fulfillment of the
Requirements for the Degree of
Master of Science

Department of Physics
University of Lethbridge
Lethbridge, Alberta, Canada

Abstract

The class of high T_c superconductors share one common structural aspect, the existence of planes of copper and oxygen ions. These planes are thought to be the source of the superconducting behaviour. They can be represented as a two-dimensional lattice of ions, which facilitates their study using numerical models. One such model is the $t - J$ model. In most studies utilising numerical models, the planes have been considered isotropic. However, recent analysis of cuprate structure has illustrated that this may not be representative of the copper oxide planes. A number of cuprate structures exhibit different phases in which the planes are not isotropic, such as the low temperature orthorhombic and low temperature tetragonal phases. This work will examine the effects of introducing anisotropy into the $t - J$ model in order to understand how these phases affect the results gained from numerical studies.

Table of Contents

List of Tables

List of Figures

List of Abbreviations

3SCF	3-Site Correlation Function
AF	Antiferromagnetic
ARPES	Angle-Resolved Photoemission Spectra
BCS	Bardeen-Cooper-Schrieffer
DMRG	Density Matrix Renormalisation Group
ED	Exact Diagonalisation
FM	Ferromagnetic
HHCF	Hole-Hole Correlation Function
HTT	High Temperature Tetragonal
IC	Incommensurate
LTO	Low Temperature Orthorhombic
LTT	Low Temperature Tetragonal
SSCF	Spin-Spin Correlation Function

List of Symbols

BE Binding Energy, defined by $BE = E_2 - 2E_1 + E_0$

$c_{i,\sigma}$ Annihilation operator for an electron of spin σ at site i.

$c_{i,\sigma}^{\dagger}$ Creation operator for an electron of spin σ at site i.

n_i Number operator, defined by $n_i = c_{i,\uparrow}^{\dagger}c_{i,\uparrow} + c_{i,\downarrow}^{\dagger}c_{i,\downarrow}$

$n_{i,\sigma}$ Number operator, defined by $n_{i,\sigma} = c_{i,\sigma}^{\dagger}c_{i,\sigma}$

$\tilde{c}_{i,\sigma}^{\dagger}$ Projected electron creation operator, defined as $\tilde{c}_{i,\sigma}^{\dagger} = c_{i,\sigma}^{\dagger}(1 - n_{i,-\sigma})$.

$\tilde{c}_{i,\sigma}$ Projected electron annihilation operator, defined as $\tilde{c}_{i,\sigma} = c_{i,\sigma}(1 - n_{i,\sigma})$.

$\vec{S}_i$ Spin operator, defined as $\vec{S}_i = S_i^x\,\hat{x} + S_i^y\,\hat{y} + S_i^z\,\hat{z}$.

S_i^x x-component of the spin operator $\vec{S}$, defined as $S_i^x = \frac{1}{2}(S_i^- + S_i^+)$.

S_i^y y-component of the spin operator $\vec{S}$, defined as $S_i^y = \frac{i}{2}(S_i^- - S_i^+)$.

S_i^z z-component of the spin operator $\vec{S}$, defined as $S_i^z = \frac{1}{2}(n_{i\uparrow} - n_{i\downarrow})$.

S_i^+ Spin-flip operator, defined as $S_i^+ = c_{i\uparrow}^{\dagger}c_{i\downarrow}$.

S_i^- Spin-flip operator, defined as $S_i^- = c_{i\downarrow}^{\dagger}c_{i\uparrow}$.

E_0^N Ground state energy of a system of N electrons.

$|E_0^N\rangle$ Ground state wave vector of a system of N electrons, of energy E_0.

Chapter 1

Introduction

1.1   Birth of a New Phenomenon

In 1911, the publication of the paper "On the Sudden Rate at Which the Resistance of Mercury Disappears" by H.K. Onnes introduced a major discovery of the 20th century [1]. By cooling mercury to temperatures lower than 4.19 K through the use of liquid helium, the electrical resistance of the material was shown to disappear completely. The material became a perfect conductor of electricity, and was later given the name "superconductor". The mystery of superconductivity was examined throughout the remainder of the century, and continues to be an active area of research to this date. Since 1911, a number of other defining characteristics of superconductors have been found. One of the more fascinating is the Meissner effect, discovered in 1933 by Meissner and Ochsenfeld [2]. It was shown in their work that materials in the superconducting state expel applied magnetic fields, which can cause a magnet to levitate above a superconducting material, as seen in figure 1.1. Other properties include the Josephson effect, which describes the current flow present at the interface between two superconductors separated by a very thin insulating layer [3]. This effect has been utilised in superconducting quantum interference devices (SQUIDs), which are currently the most sensitive devices for the detection of magnetic fields. However, technological applications of superconductors have been somewhat hindered by the extremely low temperatures required to instantiate the phenomenon.

The discovery of superconducting compounds with critical temperatures greater

Figure 1.1: Levitation of a magnet above a superconducting material immersed in liquid nitrogen.

than 30 K was a major accomplishment of the 1980's. The compounds that exhibit superconductivity in this temperature regime, hereafter referred to as high T_c superconductors, share a number of characteristics. The most notable of these characteristics is the presence of planes of copper and oxygen ions in the majority of high T_c superconductors. These compounds form a class known as the cuprate superconductors. The first such material discovered to exhibit superconductivity was $La_{2-x}Ba_xCuO_4$, found by Bednorz and Muller in 1986 to have a superconducting critical temperature of 36 K when $x = 0.15$ [4]. Previously, superconductivity was found only in certain metallic and organic compounds, most of which were poor conductors at room temperature. The highest T_c of these compounds was 23.2 K for the compound Nb_3Ge [5]. Superconducting critical temperatures had grown less than 20 K over a span of 75 years since the initial discovery of superconductivity. The increase of 13 K to 36 K was consequently met with a great deal of enthusiasm from the physics community. In addition to the T_c increase, one of the more striking aspects of this discovery was the insulating nature of the parent compound La_2CuO_4 in the normal state [6]. The ceramic constitution of the compound was also somewhat puzzling, as

previously this type of material was not known to display superconducting behaviour. Further experimental studies of cuprate materials resulted in the discovery of superconductivity in $YBa_2Cu_3O_{7-x}$ at temperatures up to 92 K [7], a very drastic increase in T_c. Given that the boiling point of nitrogen is 77 K, this allowed the attainment of the superconducting state without the use of liquid helium. But why is this important? The simple answer is cost. Nitrogen is a more abundant material than helium, and as such, liquid nitrogen is considerably cheaper and easier to manufacture than liquid helium. This makes liquid nitrogen an ideal medium for the attainment of superconductivity, which in turn marks the advancement of T_c to these temperatures as one of particular importance.

While the superconducting state was understandably the focus of the initial research of these materials, interest in other properties steadily grew as more experimental data became available. The scope of cuprate compounds now goes well beyond the realm of high-T_c superconductivity. The wealth of experimental study done on these materials has revealed a variety of interesting behaviours in phases other than the superconducting phase. In most conducting materials, it suffices to view the conduction electrons as a "sea" of non-interacting particles. This is known as the Fermi liquid [8]. The interactions between electrons, most notably the Coulomb interaction, are introduced as a perturbation to the non-interacting ground state. There are several predictions that this theory provides. Two such predictions are the temperature independence of the magnetic susceptibility, and the resistivity being proportional to T^2 at low temperatures [9]. Both of these properties are not seen in cuprates [10, 11], suggesting that the Fermi liquid description may be inadequate for these compounds. The exact nature of the normal state in these compounds has yet to be determined, and as such research on these materials remains active. The materials have also been shown to exhibit strong antiferromagnetism in certain phases, which makes the cuprate superconductors an ideal subject of studies on magnetism. In particular, the

cuprates appear to be one of the best physical examples of the Mott insulator [12](see section 1.2.1), and as such research into these two fields has been strongly linked.

Cuprate study can now be considered a field unto itself, independent of superconductivity. However, even though these compounds have been examined for almost 20 years, the existence of a predictive model for cuprates has yet to arise. The strong correlation between electrons has been one of the major obstacles in this area, as this property limits the effectiveness of simple perturbation calculations which are applicable to most Fermi-liquid type materials. The need for more research into these materials is clear, since they apply to so many different areas of condensed matter physics.

1.2 Cuprate Structure

The crystalline structure of these compounds provides the starting point for their analysis. No theoretical model can be justly applied to these materials without some advance knowledge of even the most simple crystal properties, such as lattice parameters. As one might expect, all of the cuprate materials share a similar crystal structure. As an example of this structure, the conventional unit cell of La_2CuO_4 is shown in figure 1.2. This compound has a body-centered tetragonal (bct) crystal structure, in which there are six planes of ions [13]. In terms of stoichiometry, four of these planes are LaO, while the remaining two are CuO_2. The Cu and O ions form an elongated perovskite-type structure, in which the copper ions have six nearest neighbour oxygen ions. Four of these ions lie within the CuO_2 planes, while the remaining two, known as the apical oxygens or simply O_z, lie above and below these planes on the LaO planes. The Cu-O distance in-plane is roughly 1.9 Å, while out of plane it is a much larger 2.4 Å, hence the elongated nature of the perovskite structure. This disparity results in interactions within planes being substantially stronger than those between planes. It should be noted that the picture shown of $La_{2-x}Sr_xCuO_4$,
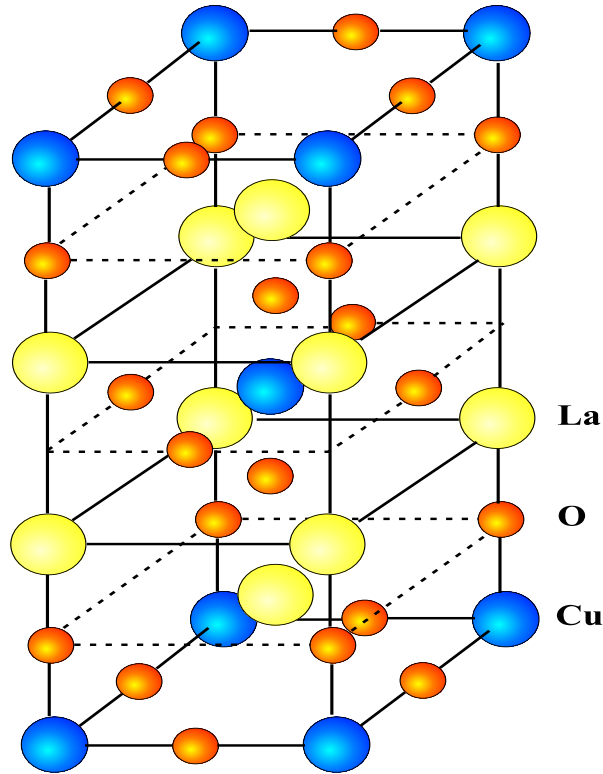
Figure 1.2: Structure of $La_4Cu_2O_8$, the parent compound of $La_{2-x}Sr_xCuO_4$. The large yellow circles denote La atoms, the medium-sized blue circles denote Cu atoms, while the small red circles denotes O atoms.

and all subsequent discussion, is based on one phase of this compound. A variety of different phases are possible for this compound, and this aspect of this material will be discussed in section 1.3. The fundamental physical characteristic that all cuprates share is the CuO_2 planes. The chemical constituents of the other planes will vary from material to material, as will the relative population of the CuO_2 planes, but the existence of these planes in all high-T_c materials is indeed the most intriguing aspect of the field. The importance of this aspect is made clear through experimental results showing the highly anisotropic nature of superconductivity within these compounds. The planes lie along the a- and b-axes of the crystal, and along these axes the resistivity of the materials is much less than along the c-axis [14, 15]. Between planes, along the c-axis of the material, conductivity is strongly suppressed. It is therefore believed

that the superconducting behaviour is limited to the copper oxide planes themselves. Thus a large number of studies on these materials have essentially ignored all other physical aspects of cuprate materials and focussed purely on the copper oxide planes. This work will do the same.

1.2.1 CuO$_2$ planes

The planes found in the cuprate superconductors are indeed their most interesting physical characteristic, and warrant further analysis. Within the planes, the copper ions have four nearest neighbour oxygen ions, while each oxygen lies between two copper ions. The copper and oxygen bonds are of mixed covalent and ionic character, and in the undoped state, the majority of copper atoms become Cu^{2+}, while oxygen becomes O^{2-} [16]. In terms of electronic orbitals, the copper ions have a filled $3p$ shell and 9 electrons in the $3d$ shell, while oxygen has a filled $2p$ shell. It should be noted that this behaviour is representative of the bulk nature of the lattice, since quantum fluctuations can alter the ionic state of each individual lattice constituent, even at absolute zero. Due to the effects of the crystal field, the degeneracy between orbitals of the same quantum number n is removed. The highest energy orbital of copper in these materials is the $d_{x^2-y^2}$ orbital, and it is this orbital that then contains a hole [17]. The highest energy orbitals in the oxygen ions are the $2p_x$ and $2p_y$ orbitals, which strongly hybridize with the copper $3d_{x^2-y^2}$ to form $3dsp$ molecular orbitals. The hole in the d shell of the Cu^{2+} ions results in these ions having a net spin of $\pm\frac{1}{2}$, while the oxygen ions are not magnetic due to their filled orbitals. The half-filled state then is characterised by a magnetic arrangement of spins, with magnetic Cu^{2+} ions containing one valence electron being mediated by non-magnetic O^{2-} ions containing two valence electrons. These mediating O^{2-} ions assist in a magnetic process known as Heisenberg superexchange [9], which couples the spins on neighbouring copper ions. Note that this magnetic interaction is in fact electronic in nature, arising from the overlap of

electron orbitals concomitant with the Pauli exclusion principle. The exchange energy of this interaction is $U = 2J\,\mathbf{S_1} \cdot \mathbf{S_2}$, which can lead to either a ferromagnetic (FM) or antiferromagnetic (AF) ground state, depending on the sign of the exchange integral J. On the copper oxide planes, J carries a positive sign, giving rise to a strongly AF ground state with Néel temperatures above room temperature. This type of magnetic behaviour was confirmed experimentally via neutron scattering data [18, 19, 20].

Given the half-filled band structure of the copper ions, one would expect La_2CuO_4, and other undoped cuprate superconductors, to be metallic conductors. However, these materials are AF insulators. The cause lies in the strong Coulomb repulsion between two electrons in the same copper orbital. Even though the Fermi level lies within a half-filled band, an energy gap Δ splits this band into an upper and lower section due to this Coulomb repulsion. The lower band is filled by electrons residing on singly-occupied Cu^{2+} ions, while the upper band is filled by electrons residing on doubly-occupied Cu^+ ions. Therefore, with a half-filled band, electrons are localised, since motion of one electron to a neighbouring site would result in an energy cost equal to the band gap. Compounds that exhibit this behaviour are known as Mott insulators. In cuprate compounds, the oxygen p-band is placed between the upper and lower d-bands due to the splitting of the copper d-band. The energy gap Δ then lies between the lower d-band and the p-band, as opposed to the upper and lower d-bands. This type of behaviour is slightly different than that seen in Mott insulators, and compounds of this nature are referred to as charge-transfer insulators. The difference between the two is seen schematically in figure 1.3. The study of Mott insulators and specifically metal-insulator transitions is an active field of study. Readers with an interest in this field can refer to a recent review article on the subject [17], and the references contained therein.
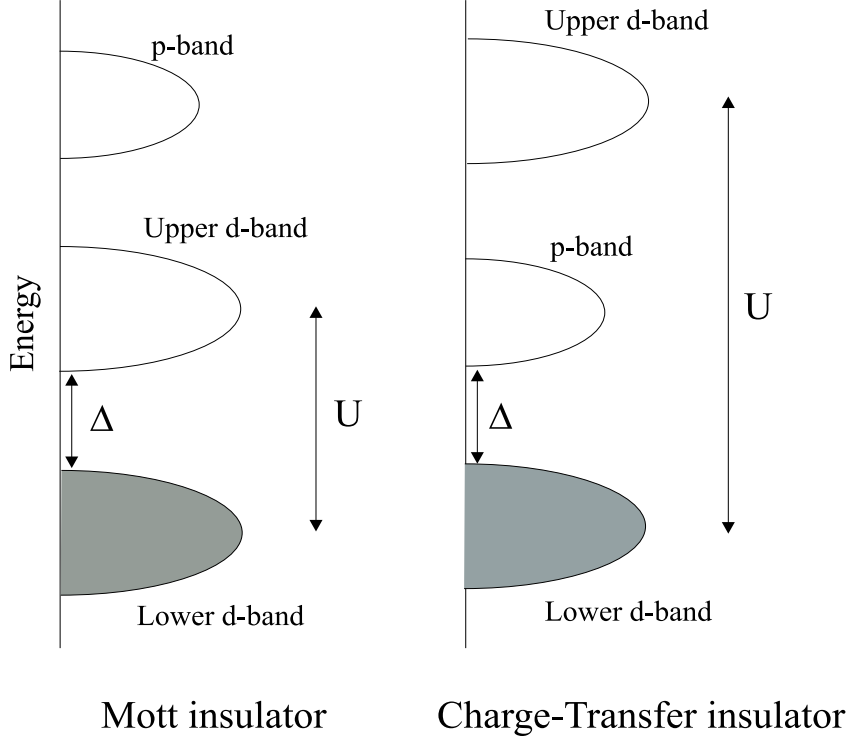
Figure 1.3: Schematic representation of Mott and charge-transfer insulators. The gray area denotes a filled orbital. The parameter U indicates the strength of the on-site Coulomb repulsion on the copper ions, while Δ is the energy gap between the highest energy occupied band and lowest energy unoccupied band.

1.2.2 Doping

The hole concentration of the planes can be altered via a process known as doping. In $La_{2-x}Sr_xCuO_4$, when La^{3+} ions are replaced with Sr^{2+} ions, electrons are removed from the planes due to the differing valency of these two ions. The electrons removed have been shown by X-ray diffraction studies to be removed from the O^{2-} ions on the CuO_2 planes [16]. This can also be viewed as introducing positively charged "holes" into the planes. It has also been shown by experimental measurement of the Hall coefficient that the positive holes are the charge carriers [21]. The effect of doping on the physical behaviour of these compounds is substantial. Superconductivity in cuprates is highly dependent on the concentration of charge carriers, as shown by the
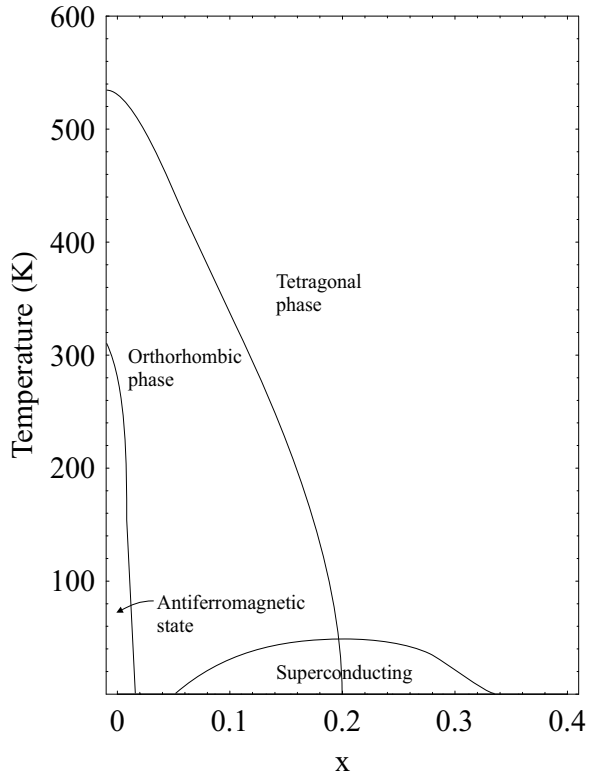
Figure 1.4: Phase diagram for $La_{2-x}Sr_xCuO_4$. These types of diagram are abundant, and can be found in such works as Imada *et al.* [17], and the references contained therein.

phase diagram of $La_{2-x}Sr_xCuO_4$ (Figure 1.4). In general, a minimum level of charge carriers is required to initiate superconductivity, with greater numbers of charge carriers resulting in a higher T_c. This behaviour holds until a critical level is achieved where T_c is maximised. Doping beyond this concentration results in suppression of T_c, until it reaches zero at some finite level of doping. Doping beyond this critical level moves the material into the overdoped regime of this phase space, where the behaviour can be modelled by Fermi liquid theory. A number of different phases have been found at the lower doping (or underdoped) regions of the phase diagram, including a spin-glass phase, a pseudogap phase, and the AF insulating phase. Most of these phases are not particularly well understood, which certainly contributes to the popularity of these materials for study.

This behaviour is consistent for most cuprates. However, the exact nature of doping can certainly differ from material to material. For materials such as $YBa_2Cu_3O_{7-x}$, electrons are removed from Cu-O chains that form off-plane, while other materials such as $Nd_{2-x}Ce_xCuO_4$ have negative charge carriers rather than positive. The result of doping remains the same, the addition of charge carriers to the copper oxide planes via alteration of the off-plane constituents. These constituents are then often referred to as the charge reservoir.

1.3 Anisotropy in CuO_2 Planes

In 1995, a study by Tranquada *et al.* [22] on $La_{1.6-x}Sr_xNd_{0.4}CuO_4$ examined the peaks found in the static magnetic structure factor $S(\vec{q})$. This factor, expressed as

$$S(\vec{q}) = \frac{1}{N_T} \sum_{j,\vec{r}} e^{-i\vec{q}\cdot\vec{r}} \left\langle E_0^N \left| \mathbf{S}_j \cdot \mathbf{S}_{j+\vec{r}} \right| E_0^N \right\rangle, \tag{1.1}$$

is a measure of the static orientation of electron spin within the material [23]. Here $\mathbf{S}_j$ is the spin operator, $|E_0^N\rangle$ represents the ground state wave vector, and N_T is the number of sites. The expected results should have included a strong peak at the $\vec{q} = (\pi, \pi)$ position, which would indicate the presence of antiferromagnetism. However, four smaller peaks were found surrounding the $\vec{q} = (\pi, \pi)$ position, at positions equally displaced from this point along the x and y directions (see figure 1.5). These types of peaks are referred to as incommensurate (IC) peaks, and are indicative of a magnetic structure which does not have the same period as the lattice. The theory put forward by the authors to explain these peaks involved the alignment of charge carriers into horizontally or vertically aligned domain walls of charge separating antiferromagnetically aligned regions of spin containing no charge. These domain walls were referred to as "stripes". Further experimental study into stripe phases led to their discovery in other cuprates. Yamada *et al.* [24] showed the existence
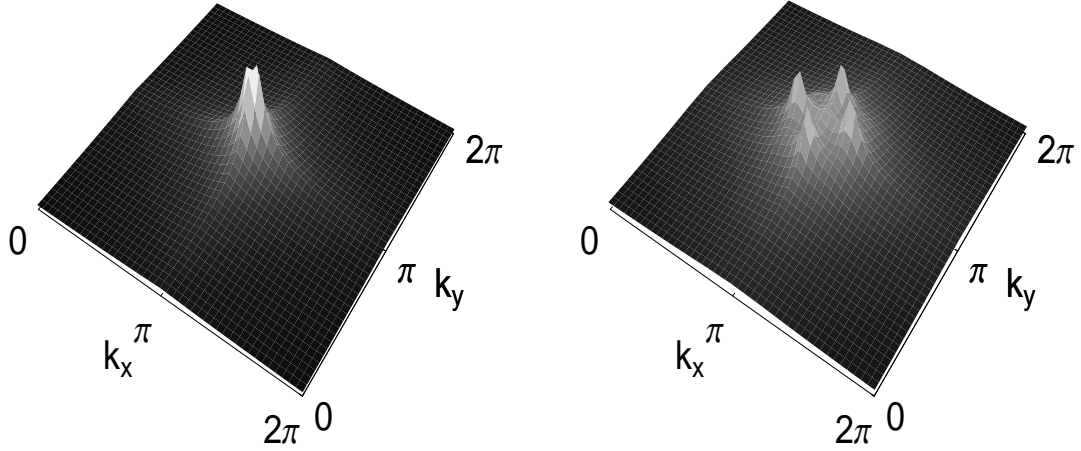
Figure 1.5: Example of commensurate and IC peaks seen in neutron scattering data. The former type of peak is seen on the left, while the latter is on the right. The peak in the commensurate case is centered at $\vec{k} = (\pi, \pi)$, while the peaks on the left are displaced from this point by 0.2π in the positive or negative x- or y-directions. The displacement of the IC peaks from the $\vec{k} = (\pi, \pi)$ point denotes the level of incommensurability, which varies by experiment, being affected by a number of factors including material and doping concentration.

of stripe behaviour in $La_{2-x}Sr_xCuO_4$ over a range of dopings in the superconducting phase of this compound, while Dai *et al.* [25] showed similar types of IC peaks in the underdoped regime of $YBa_2Cu_3O_{7-x}$. The stripes found in these materials are dynamic in nature, and represent a fluctuating state characterised by an anisotropic modulation of spin. The stripes can be seen to move throughout the lattice. This is opposed to the static stripe phase seen in $La_{1.6-x}Sr_xNd_{0.4}CuO_4$, in which the stripes become pinned by the crystal structure at $x=0.12$. The doping dependence of the incommensurability was also studied in $La_{2-x}Sr_xCuO_4$ [24] and $YBa_2Cu_3O_{7-x}$ [26], and both were found to have an approximately linear relationship with the doping concentration up to effective planar dopings of 0.10. These results suggest that there exists a stripe phase that is common to all cuprates, which would warrant further study.

A different type of stripe was found soon in the underdoped phase of $La_{2-x}Sr_xCuO_4$. Work done by Wakimoto *et al.*[27] examined the stripe phase in the spin-glass regime of $La_{2-x}Sr_xCuO_4$, at doping concentrations $0.03 \leq x \leq 0.05$. The stripe phases found here were of a slightly different nature than those found in the superconducting phase, having an orientation rotated by 45° from the previously discovered stripes. In addition, later results on the same compound [28] yielded results suggesting that the stripe phase at this range of doping was unidirectional, with the pair of IC peaks lying along the orthorhombic b-axis being much stronger than the pair found along the a-axis.

It is now widely accepted that the stripe phase is an important aspect of cuprate superconductors. This in turn begs the important question "What causes this phase?". The answer to this question is most likely to be found within the physical structure of the CuO_2 planes. As a prime example, consider the compound $La_{1.6-x}Sr_xNd_{0.4}CuO_4$, since the stripe phase was first discovered in this material. The cause of the stripe phase in this compound was attributed by the authors to the change in the crystal structure of $La_{2-x}Sr_xCuO_4$ upon Nd doping [22]. Doping of this material with Nd induces a structural phase change from the low temperature orthorhombic (LTO) phase to the low temperature tetragonal (LTT) phase at low temperature. This phase transition corresponds to a tilting of the CuO_6 octahedra along the LTO a-axis, which produces a buckling of the copper oxide planes [29]. In the LTO phase, Cu-Cu bond lengths in-plane are only slightly anisotropic, while in the LTT phase these anisotropies are enhanced. A diagram of these phases is shown in figure 1.6. Also shown in this figure is the high temperature tetragonal (HTT) phase, in which the in-plane Cu-Cu bond lengths are isotropic. $La_{2-x}Sr_xCuO_4$ is in this phase at high temperature and high doping. Typical values for a and b for this phase within this material are $a = b = 3.78$ Å[30]. The LTT phase, which shares the same axes as the HTT phase, distorts these axes so that $a \neq b$, with $b - a = 0.06$ for $La_{1.48}Sr_{0.12}Nd_{0.4}CuO_4$
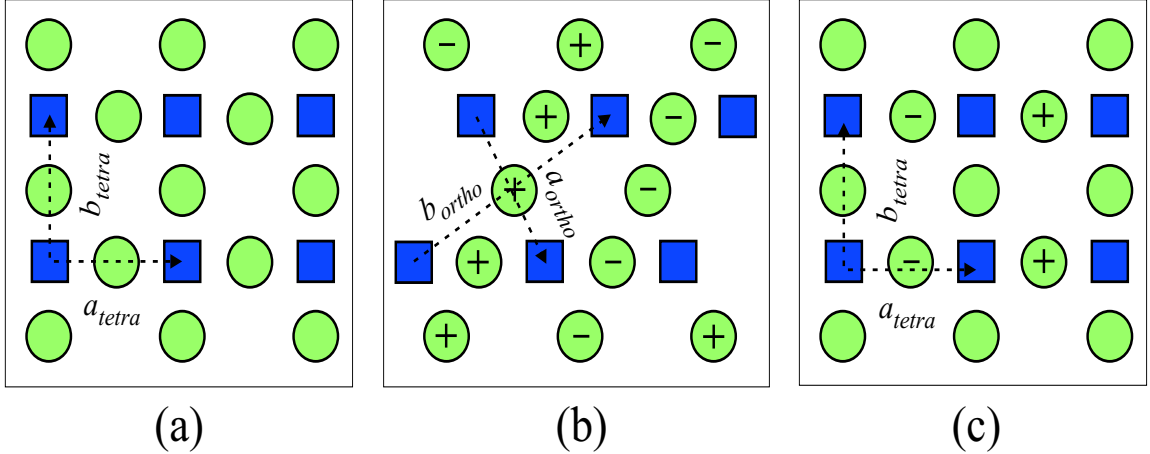
Figure 1.6: The three phases of $La_{2-x}Sr_xCuO_4$ examined in this work, which are the a) HTT phase, b) LTO phase, and c) LTT phase. The squares denote copper ions, which are all in the same plane. The circles denote oxygen ions, which are displaced either out of (+) or in to (-) the plane, or lie on the copper plane (unmarked).

[31]. The level of distortion is a function of both temperature and doping. The a and b axes within the LTO phase are oriented along the orthorhombic axes shown in figure 1.6, as opposed to the usual tetragonal axes. Typical values for the lattice parameters within this phase of $La_{2-x}Sr_xCuO_4$ are $a_{ortho} = 5.34$ Å, $b_{ortho} = 5.41$ Å[27].

The strength of the Cu-O orbital hopping is a function of bond length and bond angle, two properties which are altered upon the transitions between these phases. As a result, the most prevalent interaction on-plane becomes anisotropic, which could potentially lead to a one-dimensional arrangement of charge. Other cuprate materials exhibit this same type of transition. For example, a similar type of phase transition occurs in $YBa_2Cu_3O_{7-x}$ at $x = 0.30$ [32], but the change in bond length associated with this change is comparatively small.

Certainly the study of anisotropy in cuprates has been studied most fervently in the context of stripes. However, the effects of anisotropy in the planes may have a much broader scope than the stripe phase. The effects of anisotropic exchange interactions on the physical properties of the CuO_2 planes will be the focus of this

work. In order to study these effects, numerical simulations on a two-dimensional lattice will be used. These simulations will be carried out within the framework of the $t - J$ model, which will be introduced in Chapter 2. The model will incorporate two different types of anisotropy, one of which will be suitable for the 45° stripes seen in underdoped $La_{2-x}Sr_xCuO_4$, while the other will be suitable for the 90° stripes seen in $La_{1.6-x}Sr_xNd_{0.4}CuO_4$. Results using each of these types of anisotropy will be presented in chapters 3 and 4, respectively.

Chapter 2

The t-J Model

2.1 Introduction

The primary focus of this chapter will be to examine the origins of the $t - J$ model, and discuss the agreement between its results and those gained from experiment. The data in this work will all be generated using this model. The current state of the model, its merits and shortcomings, will also be discussed. The model is based on the Hubbard model, which itself is based on the tight-binding approximation. These two theories will be discussed first in order to provide the theoretical background for the $t - J$ model. Extensions to this base model will then be discussed.

2.2 Analytical Analysis of Cuprates

There exists in the field of condensed matter physics a vast array of theoretical procedures that one may employ to garner knowledge of crystalline materials. Which of these methods is the most appropriate for cuprate materials is, of course, a matter of contention. However, there is a degree of consensus in this issue in regard to the appropriate starting point. The strong on-site Coulomb repulsion present in these materials localises electrons, as discussed in section 1.2.1. Thus a model that explicitly accounts for this tendency towards localisation would be appropriate. Models that account for this tendency are known as tight-binding models.

2.2.1 Tight-binding approximation

The tight-binding approximation, also referred to as the generalised tight-binding method, relies on construction of a basis set of localised one-electron wave functions. The many body wave functions of a collection of atoms are then represented by a linear combination of these atomic wave functions, and as such, the model has also been named the linear combination of atomic orbitals method. In general, one constructs a wave function of the type

$$|\psi\rangle = \sum_i a_i |i\rangle, \tag{2.1}$$

where the states $|i\rangle$ are the localised atomic orbitals. The coefficients a_i satisfy the normalisation condition $\sum_i |a_i|^2 = 1$. In this basis, the Hamiltonian matrix elements assume the form $H_{ij} = \langle i|H|j\rangle = \int \psi_i^*(r) H \psi_j(r)\, dV$. The diagonal terms $H_{ii} = \epsilon_i$ are the on-site energies of the electrons on their respective sites, while the off-diagonal terms $H_{ij} = t_{ij}$ represent hopping terms between sites i and j. Determination of these hopping elements can be somewhat complex, given the nature of the atomic wave functions $|i\rangle$, which are solutions to the spherically symmetric single-electron Hamiltonian. These solutions can be found in any introductory quantum mechanics text, and are generally presented as products of a radial function and a spherical harmonic function. Even though evaluation of the atomic orbitals themselves poses no great difficulty, evaluation of the overlaps between wave functions such as these is almost a field unto itself, and in general requires a large amount of computational work. For now it will suffice to say that these hopping elements are generally parameterised, and in most cases focus only on nearest neighbour hopping between sites. The result is then a set of linear equations involving parameters describing the energies of various sites and the hopping between these sites. These equations can then be solved and the band structure of the lattice can be evaluated. The critical assumption in this approximation is that the lowest occupied states of the material

are bound states, and that the unbound states represent much higher energy excited states. These excited states can then be neglected.

Note that this description contains only a formulism of the kinetic energy of the electrons, as well as their on-site energies. The potential energy can be included by the use of additional terms, the most important of which is the Coulomb repulsion. This repulsion can be modelled by incorporating a V term into the diagonal elements of the Hamiltonian. This term will add to the energy of a given state when electrons exist on nearby orbitals. The $1/r$ dependance of the term implies that the potential from a single electron would affect sites at large r, but in general the potential is restricted to at most nearest neighbours. This is justified physically by the screening effect of the ion cores and the electrons on this potential.

2.2.2 The Hubbard model

Now consider a case of the tight-binding model which only includes the highest energy occupied orbitals present at each site, and includes a short-range Coulomb repulsion term U that only affects electrons in the same orbital. The Hamiltonian corresponding to this model is

$$H = -\sum_{i,j,\sigma} t_{ij}(c_{i\sigma}^\dagger c_{j\sigma} + c_{j\sigma}^\dagger c_{i\sigma}) + U\sum_i n_{i\uparrow}n_{i\downarrow}, \tag{2.2}$$

where $c_{i\sigma}^\dagger$, $c_{i\sigma}$ are the creation and annihilation operators, respectively, of an electron at site i with spin σ, $n_{i\sigma} = c_{i\sigma}^\dagger c_{i\sigma}$ is the number operator, and t_{ij} is a parameter measuring the orbital overlap between sites i and j. This model is the well-known Hubbard model [33], which has been the topic of a great deal of study. Although very simple, it can aptly describe the dominant physics in materials that exhibit strong correlation between electrons, such as Mott insulators. Materials showing a strong tendency towards a magnetic phase such as ferromagnetism or antiferromagnetism are also well described by this model. Given that the cuprates are in both of these classes of material, an extension of this model was applied to the copper oxide planes by V.

Emery in 1987 [34]. This work considered the three highest energy orbitals occupied in the low-temperature limit of the CuO$_2$ planes, the Cu 3d$_{x^2-y^2}$ orbital, and the O 2p$_x$ and 2p$_y$ orbitals. The model is known as the three-band Emery model. It was postulated by Emery that the holes doped onto the O^{2-} ions can couple with one another via the local Cu spins, producing transition temperatures above 30 K. Since this work, the three-band Hubbard model has become the basis of many theoretical works on cuprates. The simplicity of this model does lend it some appeal, but this simplicity is offset somewhat by its detail, which enlarges the size of the Hilbert space it considers. Given that each site in the lattice can hold 0, 1, or 2 electrons, and that singly occupied sites can have spin up or spin down electrons, the sheer volume of states can severely limit the size of lattices that can be analysed with this model. This in turn creates difficulties with extrapolating the results to the bulk limit of an infinite lattice.

2.2.3 The t-J model

While the three-band Hubbard model is certainly a detailed and fairly accurate description of the electronic structure of the planes, simplifications to it have been made in order to alleviate the complexity caused by its detail. Prior to the introduction of the three-band model, Anderson proposed that a one-band Hubbard model could be appropriate for the cuprates [35]. The one-band model proposed in this work contains singlet pairs of holes, formed between a hole on a copper ion and a hole on one of the adjacent oxygen ions. The benefit of this assumption is that each primitive CuO$_2$ cell in the planes can be represented as one site, which greatly reduces the number of states that need to be considered. However, it is unclear whether the one-band model is sufficient to describe the low-energy physics of the system. Theoretical work supporting the one-band model was presented by Zhang and Rice in 1988 [36]. This

work examined all the states possible in a system containing a single Cu^{2+} ion containing one $3d$ hole and four neighbouring O atoms, one of which contained a single $2p$ hole. By explicitly accounting for the phase of the Cu $3d_{x^2-y^2}$, O $2p_x$, and O $2p_y$ orbitals, the singlet state formed between the O hole and the Cu hole was found to have an energy of $-15.4t$, roughly $15t$ less than the triplet state. If one assumes that holes doped into the planes can be represented by these singlet states, then the O orbitals surrounding a Cu site can be expressed with one band instead of two. The model can be further reduced by assuming that $U \gg t$, ridding the model of Cu^+ and Cu^{3+} ions. By applying these two approximations, the three-band model can then be reduced to a one-band model, with the holes being doped onto the O^{2-} ions within the planes. The spin of these holes is opposite that of the hole occupying the central Cu^{2+} ion. It is then these local singlets that propagate through the lattice carrying charge. The Cu^{2+} holes appear rigid, while the O holes appear to move throughout the lattice.

One consequence of this reduction is the addition of magnetic exchange terms, introduced in the perturbation theory upon elimination of the doubly occupied states. The most prominent of these terms is the nearest neighbour copper-copper magnetic exchange term, which appears as

$$J \sum_{<i,j>} \left(\mathbf{S_i} \cdot \mathbf{S_j} - \frac{n_i n_j}{4} \right). \tag{2.3}$$

Here the sum over $< i, j >$ implies that each bond is only counted once. This term couples the spins on neighbouring coppers, resulting in the AF configuration of spin present in the planes, with positive J. This term represents the same type of magnetic interplay discussed in section 1.2.1. The magnitude of the parameter J can be expressed in terms of the Hubbard parameters t and U by the relation $J \approx 4t^2/U$. Proof of this relation is given in Appendix A.

The result of the approximations introduced by Zhang and Rice is the $t-J$ model, which describes a lattice with a single site per unit cell with two interactions present, represented by the parameters t and J. Since it is assumed that $U \gg t$, all the copper sites contain a single electron, and all holes doped into the planes reside on oxygen ions. The effective sites then have three possible states. If a hole is present on a neighbouring oxygen ion, then the local singlet formed with the copper hole can be represented by a spinless vacancy on the site. If a local singlet is not present, the spin of the electron is represented as either up or down. Again, it should be stressed that a "hole" on a site in this lattice does not simply correspond to a hole on a copper site. All sites in the lattice have holes, regardless of which state described above is present. The Hamiltonian of the $t-J$ model can then be written as

$$H = -t \sum_{<i,j>,\sigma} (\tilde{c}^{\dagger}_{i,\sigma} \tilde{c}_{j,\sigma} + h.c.) + J \sum_{<i,j>} \left(\mathbf{S_i} \cdot \mathbf{S_j} - \frac{n_i n_j}{4} \right), \qquad (2.4)$$

where the index j is limited to nearest neighbour sites of i. The operators $\tilde{c}^{\dagger}_{i,\sigma}$ and $\tilde{c}_{j,\sigma}$ are the projected Fermion creation and annihilation operators. The relations $\tilde{c}^{\dagger}_{i,\sigma} = c^{\dagger}_{i,\sigma}(1 - n_{i,-\sigma})$ and $\tilde{c}_{j,\sigma} = (1 - n_{j,-\sigma})c_{j,\sigma}$ ensure that double occupancy of sites is not allowed. $\mathbf{S_i}$ is the spin operator, while $n_i = c^{\dagger}_{i,\uparrow}c_{i,\uparrow} + c^{\dagger}_{i,\downarrow}c_{i,\downarrow}$ is the number operator. The number operator simply equals 1 if an electron is present at the site, and 0 otherwise.

The elimination of oxygen sites and doubly occupied copper sites results in a large reduction of the Hilbert space when compared to the Hubbard model. As an example of this, consider a lattice involving four copper sites at the corners of a square, with four intervening oxygen ions. In the half-filled case, with the total spin S fixed to $S=0$, the Hubbard model has 784 states. In contrast, the $t-J$ model has only 6 states. This makes the $t-J$ model a suitable model for study on larger lattices. The results from these lattices can then be extrapolated to the bulk limit with the use of

periodic boundary conditions.

2.2.4 Parameter values

The hopping parameter t represents the ability of the singlet state centered about one CuO_2 cell to hop to an adjacent site. This parameter is based on the Hubbard parameters U_d, t_{pd}, and ϵ_p, where the subscripts p and d denote oxygen $2p_x$, $2p_y$ and copper $3d_{x^2-y^2}$ orbitals, respectively. Zhang and Rice [36] estimated the relation between effective singlet hopping parameter t and the Hubbard parameters as $t = -1.5t_{pd}^2/(U - \epsilon_p)$. Values for the Hubbard model parameters are numerous, and can be obtained through the use of a wide variety of methods. Feiner *et al.* [37] used a cell perturbation method on the three-band Hubbard model to obtain the parameter set $U_d = 7t_{pd}$, $\epsilon_p = 2.7t_{pd}$, and $t_{pd} = 1.3$ eV. These parameters result in $t = 368$ meV according to the relation given by Zhang and Rice. Other band structure calculations of the Hubbard parameters give $U_d = 5.7t_{pd}$, $\epsilon_p = 2.1t_{pd}$, and $t_{pd} = 1.4$ eV [38]. These numbers are similar to that of Feiner, with the resulting value for t being 576 meV. Belinicher *et al.* [39] used these Hubbard parameters in a reduction of the full three-band Hubbard model to the $t - t' - J$ model, and concluded that $t = 427$ meV.

The exchange integral J has been estimated in a variety of ways, both theoretical and experimental, for a number of cuprate compounds. Experimental fits for La_2CuO_4 have resulted in values of $J = 133$ meV [40], $J = 128$ meV [41], and $J = 125$ meV [42], using different experimental techniques. Theoretical procedures yield similar values. One can attempt to approximate J by evaluating the orbital overlaps, as discussed in section 2.2.1. Values gained from such attempts place J between 100 and 140 meV for most cuprates [43]. This approach can be quite complex, and relies on evaluation of difficult integrals. As such, this method has not been used extensively. A more popular method of evaluating the exchange integral within the $t - J$ model is to begin with the Emery model (see section 2.2.2) and map the model onto the $t - J$ or

21

extended $t - J$ model. This has resulted in values of 126 meV [39] and 115 meV [44].

The generally accepted "realistic" values for t lie somewhere between 300 and 500 meV, with J being between 120 and 140 meV. If t is used as the energy scale, then values for J/t lie somewhere between 0.25 and 0.45. There have been a number of studies using $J = 0.3t$, $J = 0.35t$, and $J = 0.4t$. This work will primarily use $J = 0.4t$. It should be noted that the *ab initio* calculations done using the Emery model rely themselves on approximations to the Emery parameters. These parameters include the on-site and next-site Coulomb repulsion terms, as well as the direct Cu-O and O-O orbital hopping terms. Determination of these parameters is generally conducted in the same way as the t parameter, by some sort of fitting to experimental data that results in a range of values for the parameters. Thus, the values for t and J gained by reducing the Emery model to the $t - J$ model represent an approximation which itself is based on an approximation.

2.3 t-J Model Results

To this point in time, it remains controversial as to whether the $t - J$ model can accurately describe the low-temperature behaviour of the high-T$_c$ superconductors. The model has reproduced many experimentally seen properties in the underdoped region, including the strong quasiparticle peak found in angle-resolved photoemission spectroscopy (ARPES) results, long-range AF correlations, and phase separation of charge carriers. These results will be explained in detail in the following sections.

2.3.1 Spectral properties

The spectral properties of cuprates are generally associated with the spectral function $A^{(-)}(\vec{k}, \omega)$ and the density of states $N^{(-)}(\omega)$. These quantities are defined as

$$A^{(-)}(\vec{k}, \omega) = \sum_n |\langle E_n^{N-1} | c_{\vec{k}, \sigma} | E_0^N \rangle|^2 \, \delta(\omega - E_0^N + E_n^{N-1}) \qquad (2.5)$$

$$N^{(-)}(\omega) = \sum_{\vec{k}} A^{(-)}(\vec{k}, \omega), \qquad (2.6)$$

where E_0^N and $|E_0^N\rangle$ are the ground-state energy and wave function, respectively, and E_n^{N-1} and $|E_n^{N-1}\rangle$ are the nth excited energy and wave function of the eigenstate when one electron is removed. Evaluation of these quantities numerically relies on the use of the continuous fraction expansion [23], which involves a large number of Lanczos iterations. Experimentally, $A^{(-)}(\vec{k}, \omega)$ is measured using ARPES, while $N^{(-)}(\omega)$ is the angle-integrated intensity of this data. Due to the availability of ARPES data, the spectral function is a well-studied quantity of the $t-J$ model. Comparison of $t-J$ model results to experimental ARPES data has produced strong agreement with the quasiparticle peak, the coherent part of the spectrum. However, the incoherent part is missing from the $t-J$ data. Numerical results for the energy dispersion using the $t-J$ model have produced similarities with experimental data along the $\vec{k} = (0,0)$ to $\vec{k} = (\pi, \pi)$ cut of reciprocal space [45, 46]. However, there are discrepancies along the $\vec{k} = (\pi, 0)$ to $\vec{k} = (0,0)$ line, and the $\vec{k} = (\pi, 0)$ to $\vec{k} = (0, \pi)$ line. The latter shows a very flat dispersion in the numerical results [45], as opposed to the well-defined peak of the experimental results [46]. The agreement between these results has been augmented by inclusion of higher order hopping terms into the model, as discussed in section 2.4.

2.3.2 Magnetism

The magnetic properties of the cuprates are in some cases well understood, and have been well represented by theoretical models. The existence of an AF state in the low temperature, low doping region of the phase diagram has been well supported in theoretical models. Most studies of magnetic properties focus on the static magnetic structure factor $S(\vec{q})$, defined in section 1.3, since this quantity is easily measurable experimentally via neutron scattering. The strength of the AF order within the lattice can be ascertained with this function by examining the weight of $S(\vec{q})$ at

$\vec{q} = \mathbf{Q} = (\pi, \pi)$. A strong peak at this wave vector indicates the presence of AF order. Early experimental results from Cheong *et al.* [47] showed the existence of IC magnetic peaks in $La_{2-x}Sr_xCuO_4$ at $x = 0.075$ and $x = 0.14$. Subsequent theoretical studies of $S(\vec{q})$ within the $t - J$ and Hubbard models also showed the existence of IC peaks in $S(\vec{q})$ around $\mathbf{Q}$ [48, 49]. These peaks diminished as the doping concentration x was increased, with $S(\mathbf{Q})$ scaling as $1/x$. Thus the long range AF tendency of the model was shown to diminish as the doping is increased, as has also been seen experimentally. This agreement between experimental and theoretical results strongly suggests that the magnetic portion of the model can aptly mimic the copper oxide planes.

2.3.3 Charge ordering

The behaviour of the charge carriers on the planes carries a great deal of interest, since the charge carriers are responsible for the superconducting behaviour. One of the most discussed topics in this area is the debate over phase separation, and whether this phenomenon is seen in the $t - J$ model. Phase separation implies a congregation of the holes into zones, with few or no holes in the spaces between these zones. The real-space placement of the holes within the model can be evaluated through the use of the hole-hole correlation function (HHCF) [23], defined as

$$C_{hh}(\vec{r}) = \frac{1}{N_h} \sum_i \left\langle E_0^N \left| (1 - n_i)(1 - n_{i+\vec{r}}) \right| E_0^N \right\rangle. \tag{2.7}$$

The results from this function are highly sensitive to the value of the parameter J. It has been shown that phase separation occurs within the model for $J > 0.45$, while for $J < 0.18$ the holes separate as far apart as possible [50]. Between these values, the holes tend to form bound pairs at distances of $\sqrt{2}a$ [50, 51]. For most compounds, J has been measured to be in the range of $0.3t$ to $0.4t$, indicating that

bound pair formation is the preferred behaviour of the charge carriers within the model at realistic values of J. This result is encouraging for the validity of the model, since bound pair formation is one of the key aspects of superconductivity. Charge ordering has also been studied in the context of stripes. As discussed in section 1.3, the current explanation for the charge and spin modulations seen in $La_{1.6-x}Sr_xNd_{0.4}CuO_4$ is the orientation of the charge carriers into domain walls. This type of behaviour has been seen in the $t - J$ model using Density Matrix Renormalisation Group (DMRG) techniques on four-leg ladders [52].

2.4 Extended t-J Model

As noted in section 2.3.1, the agreement between the numerical and experimental results for the energy dispersion has been augmented through the use of additional hopping terms. These terms allow motion of holes to sites at further distance than nearest neighbour, and arise from the reduction of the Hubbard model to the t-J model in a similar manner as the magnetic exchange. The most prominent of these terms is t', a second order term which allows holes to hop to next-nearest neighbour sites. The importance of this parameter in reproducing experimental ARPES results was shown by Nazarenko *et al.* [53].

There is some controversy surrounding these extended parameters. The effect of t' on the stripe phase has been tested using Hartree-Fock [54], DMRG [55], and exact diagonalisation (ED) [56] calculations. The results clearly show a suppression of stripe-like behavior for $t' < 0$, and stabilization of stripes for $t' > 0$. It has been shown previously that $t' < 0$ for hole doped cuprates and $t' > 0$ for electron doped materials [57, 58]. Also, experimental work using ARPES on $Sr_2CuO_2Cl_2$ has provided approximate values for t' that are definitely negative for the hole doped materials [53]. Since a negative t' suppresses stripes in the $t - J$ model, an additional mechanism is required to restabilize the stripes in the presence of a realistic t' parameter.

This mechanism could be a higher order hopping term t'' that allows hole motion to next-next-nearest neighbour sites a distance of $2a$ away. Even though t'' has values comparable to t' and J [39], and the inclusion of t'' was necessary for matching the extended $t - J$ model's spectral function to the experimental ARPES data [59], very little work has been done with this parameter to date, particularly in the context of stripes.

Values for the extended parameters t' and t'' have been evaluated in much the same way as the parameters t and J. A fit of the extended $t - J$ model by Xiang and Wheatley [59] to the ARPES data of $Sr_2CuO_2Cl_2$ gave the following set of parameters: $J = 0.43t$, $t' = -0.34t$, $t'' = 0.23t$. Later work by Leung et $al.$ [60, 61] to the ARPES data of $Sr_2CuO_2Cl_2$ gave the following set of parameters: $J = 0.3t$, $t' = -0.3t$, $t'' = 0.2t$ and work by Kim et $al.$ [62] with high resolution ARPES data obtain values of: $J = 0.40t$, $t' = -0.34t$, $t'' = 0.23t$ in agreement with Xiang and Wheatley [59]. The values for these parameters vary for each material, since the orbital overlaps are different in each case. However, the differences are quite small. For $La_{2-x}Sr_xCuO_4$, the parameters have been found to be somewhat less than for $Sr_2CuO_2Cl_2$, with $0.3t \leq J \leq 0.4t$, $-0.2t \leq t' \leq -0.1t$, and $|t''| < |t'|$ [37, 63]. In general, values for the extended parameters for all copper oxide planes lie within the range $-J < t' \leq -0.1t$ and $0 < t'' \leq |t'|$. The extended parameter values used in this work will be within this range.

2.4.1 Anisotropic models

The structural anisotropies discussed in section 1.3 can be represented in theoretical models via anisotropic hopping parameters. The LTT phase of $La_{2-x-y}Nd_ySr_xCuO_4$ displays a disparity between the x- and y-directions, suggesting the need for anisotropic t and J parameters. The effects of these parameters on the $t - J$ model has been examined using DMRG [54] and Monte Carlo [64] methods. These studies used

anisotropic t and J parameters within the context of the standard $t - J$ model to examine the spin incommensurability and charge correlations. These properties are the primary signatures of stripes. The results indicate that the anisotropic model can enhance the incommensurability in the spin structure factor, while results for the charge ordering signatures are inconclusive. The work done on the spin-glass regime of $La_{2-x}Sr_xCuO_4$ focussed on the diagonal spin stripes of this compound [27]. In this doping regime, the compound is in the LTO phase, which exhibits a small anisotropy between the $\hat{x} + \hat{y}$ and $\hat{x} - \hat{y}$ directions. The diagonal stripe nature coupled with the structural anisotropy suggest that an anistropic t' term would be appropriate for this level of doping. Recent work using such an anisotropic t' term suggests this type of anisotropy may enhance the spin incommensurability and one-dimensional charge correlations [65].

Typically these anisotropies are ignored in theoretical models, since in most cases the degree of anisotropy is small. However, the effects of even small anisotropies have yet to be shown within the context of theoretical models. The extended $t - J$ model was treated in a similar way in early studies of CuO_2 planes, with the extended parameters being ignored due to the belief that the magnitude of these parameters is much smaller than t. The strong effects of these parameters on the model has been clearly shown, suggesting that the presence of even small changes in the parameters may result in significantly different results from the model. This type of anisotropic model will be the focus of this work. The precise values for the parameters and levels of anisotropy will be discussed in the relevant chapters.

2.5 Numerical Analysis of Cuprates

The use of the tight-binding models allows theoretical cuprate analysis to be reduced to the study of lattices of ions. The copper oxide planes can be represented as small clusters of copper and oxygen sites, each of which can have a fixed number of

possible states. The interactions between these states can be modelled using numerical parameters. These clusters and their corresponding states can easily be represented using computers, and can be solved using numerical methods. One such method is the exact diagonalisation approach. In this method, the entire Hamiltonian of the Hilbert space corresponding to a given set of quantum numbers is evaluated and subsequently diagonalised. This gives the exact energy and ground state wave vector for a given lattice. The method is somewhat restrictive in terms of the size of lattices it can handle, since the Hamiltonian matrix is of dimensions $N_S \times N_S$, where N_S is the size of the Hilbert space being examined.

There are a variety of methods which can be employed to carry out the diagonalisation of the Hamiltonian matrix. One of the more commonly used methods is the Lanczos technique. In this method, a special basis is constructed in which the Hamiltonian has a tridiagonal representation. This procedure is done in an iterative manner. Once the Hamiltonian is in this tridiagonal state, it can be easily diagonalised using standard routines, such as bisection. To obtain the tridiagonal representation, one begins with an initial random wave vector that serves as the trial wave vector. With each iteration, the Hamiltonian is applied to the trial vector and the resulting basis is orthogonalised. Each iteration gives values for one row of the tridiagonal matrix, and a value for the energy can be extracted by diagonalising the current form of this matrix. This results in a continued improvement of the energy and trial wave vector with each iteration, until convergence in the energy is reached. For calculations within the $t - J$ model, this typically requires not more than 100 iterations. A more complete description of this technique can be found in a number of works [66, 23, 67]. It should be noted that the Lanczos technique is generally used at $T = 0$ K. It is possible to use the Lanczos technique at higher temperatures using the Finite Temperature Lanczos Method [68]. This technique is generally more time-consuming than the Lanczos method, but is able to examine the temperature

dependence of calculated quantities. The standard Lanczos method will be used in this work.

2.5.1 Finite lattices

Evaluation of the properties of cuprate compounds using numerical models requires a model of the CuO_2 plane. A simple and appropriate model for this is a two-dimensional square lattice. For multiband models involving Cu-O interactions, such as the three-band Hubbard model, each site on the lattice represents a copper or oxygen ion, in alternating fashion. For single band models such as the $t - J$ model, each site can represent a single CuO_2 cell.

Within the $t - J$ model, each site can contain one of three possible states. The size of the Hilbert space defined by a given lattice is then equal to 3^N, where N is the number of sites within the lattice. This creates a staggering number of states for even a small sixteen site lattice, which is one of the smallest such lattices studied using numerical models. The number of states can be reduced by fixing the total S^z spin and total charge Q contained within the system. The fixing of these quantities is justified by the absence of either a spin-flip term or a charge creation term within the $t - J$ Hamiltonian. Therefore each section of the Hamiltonian defined by a given set of quantum numbers for Q and S^z comprises an independent system, which can be examined separately. The total charge Q is set to mimic a given doping concentration, while S^z is commonly set as close to zero as possible, representing an AF situation.

In order to represent an infinite lattice, periodic boundary conditions may be used in conjunction with a finite lattice. The wave function is made periodic through the use of Bloch's theorem [69]. This theorem shows that the solution of the wave equation for a periodic potential is a product of a periodic function $u(\vec{r})$ multiplied by a plane wave of the form $e^{i\vec{k}\cdot\vec{r}}$. The wave function found through analysis of the finite cluster of sites can then be applied to the infinite lattice. The relevance of

these small clusters to the cuprates themselves is justified by the short correlation length of the superconducting pairs. Pairing in cuprates has been shown to occur over just a few lattice spacings, as opposed to the longer range pairing found in typical Bardeen-Cooper-Schrieffer (BCS) superconductors. Thus the size of the cluster need not be excessive in order to encompass the pertinent physics of the planes. However, the size and shape of the finite lattice can rather unfortunately have a significant impact on the results gained from numerical studies. These finite size effects are the main drawback of the exact diagonalisation technique, which is restricted to small clusters where these effects are most dramatic. Currently the largest size of cluster to be studied using this technique is thirty two sites [60, 70], while studies on clusters less than sixteen sites are scarce. The evolution of the Hilbert space to exponentially greater sizes as the boundaries of the cluster are widened is a concern that can be compensated for by the availability of faster and better computer systems.

One of the consequences of the imposition of a finite lattice is the discrete nature of the allowed wave vectors $\vec{k}$. According to the Bloch theorem, the wave function satisfies the equation

$$\Psi_k(\mathbf{r}) = e^{i\mathbf{k}\cdot\mathbf{r}}u_k(\mathbf{r}). \tag{2.8}$$

A translation through N sites in a given direction should leave the wave function unchanged, so that

$$e^{i\mathbf{k}\cdot\mathbf{a_1}N} = 1, \tag{2.9}$$

where a_1 is the lattice spacing in that direction. This equation has N separate solutions, of the form

$$\mathbf{k_1} = \frac{j}{N}\,\mathbf{g_1},\ j = 0, 1, \ldots, N-1\,, \tag{2.10}$$

where $\mathbf{g_1}$ is a reciprocal lattice vector. Therefore the number of wave vectors N_k equals the number of sites within the finite lattice N.

This discrete set of wave vectors can prove to be an important hindrance when

comparing results gained from numerical study with those gained from experiment. For example, the energy dispersion relation is typically presented in experimental studies along the $\vec{k} = (0,0) \rightarrow \vec{k} = (\pi, 0)$, $\vec{k} = (0,0) \rightarrow \vec{k} = (\pi, \pi)$, and $\vec{k} = (\pi, 0) \rightarrow \vec{k} = (\pi, \pi)$ lines. Several of these finite lattices have only two or three allowed wave vectors along these lines. Fits to the experimental data can then be quite difficult to create. Proof of IC magnetic peaks within the model is also hampered by this discrete set of wave vectors. The IC peaks in $La_{1.6-x}Sr_xNd_{0.4}CuO_4$, for example, lie approximately at the $\vec{k} = (\frac{7}{8}\pi, \pi)$ and $\vec{k} = (\pi, \frac{7}{8}\pi)$ positions within the first Brillouin zone, wave vectors which are not found in most of the square clusters listed. Proof of these peaks using numerical studies of small lattices is therefore more implicit than explicit. The lack of the $(\frac{\pi}{2}, \frac{\pi}{2})$ wave vector in a number of square lattices is also a concern, as this has been shown to be the proper ground state of the one hole model [71].

Chapter 3

LTO Phase

3.1   Introduction

As discussed in section 1.3, a number of cuprate materials exhibit the LTO structure. This phase is depicted in figure 1.6. The most prominent of these is $La_{2-x}Sr_xCuO_4$, which is in this phase at low doping and low temperature. In most numerical studies employing the t-J model, this phase has been considered isotropic. This is most certainly true for the standard t-J model, which considers only nearest neighbour exchanges. However, the LTO phase is anisotropic for all next-nearest neighbour exchanges. This can be modelled numerically via the use of an anisotropic t' parameter. The effects of including this anisotropy in the extended t-J model will be the primary focus of this chapter. To this end, a variety of measurable quantities will be examined with and without the use of anisotropy, to illustrate the effects of this change.

Three sets of values for the parameters t' and t'' will be used throughout this chapter. t' shall be set to values of $-0.1t$ and $-0.3t$, while a case using $t' = -0.3t$ with $t'' = 0.2t$ will also be examined in order to investigate the effects of t'' on an anisotropic t' model. The anisotropy in t' will vary from $\delta t' = 0.001t$ to $\delta t' = 0.01t$, where the relation between the isotropic t' and the anisotropic t'_{x+y} and t'_{x-y} is given by $t'_{x+y} = t' + \delta t'$, $t'_{x-y} = t' - \delta t'$.

In order to study the LTO phase, a square cluster of twenty sites will be used. This cluster is pictured in figure 3.1. The twenty-site cluster is the largest square cluster available that provides the ability to align charge in a stripe. The larger
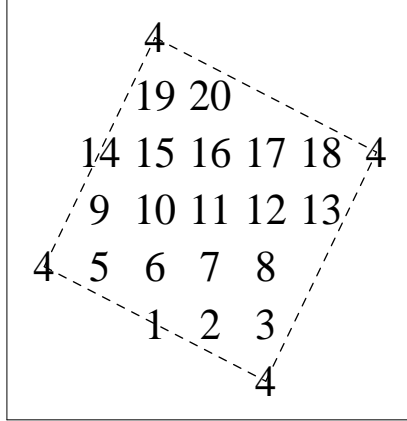
Figure 3.1: The twenty-site cluster that will be used in this chapter. Dashed lines denote the cluster boundaries. The site labelled as 4 is repeated to show the translation vectors for this cluster.

twenty six-site square cluster can be represented as a single staggered row of twenty six sites, which makes it unable to reproduce a striped arrangement of charge. The square thirty two-site cluster is currently beyond the limitations of the computing hardware available to the author of this work. The twenty-site cluster is then the largest available choice. Although this cluster is quite small, the two-hole ground state of this cluster is found at $\vec{k} = (0,0)$ for a wide range of parameters. This is representative of Cooper pairing, since Cooper pairs are comprised of two charge carriers of wave vector $\vec{k}$ and $-\vec{k}$.

3.2 Binding Energy

The preference for holes on the planes to form bound pairs can be measured by the binding energy, defined as

$$BE = E_2 - 2E_1 + E_0, \tag{3.1}$$

where E_n is the energy of the $n-$hole system. This quantity simply compares the energy of a system containing two independent holes with that of a two-hole system. A negative value indicates that the holes prefer to form a bound state, rather than

act independently. The issue of binding is quite relevant to superconductivity, as the formation of Cooper pairs is one of the primary aspects of the superconducting phase. Results for the $t - J$ model have shown binding energies that are strongly negative for realistic parameter values. Given that the changes in the parameters of the model are small when the anisotropy is included, one would not expect a great change in the energy of the system. This hypothesis is confirmed in Table 3.1.

t'	t''	$\delta t'$	BE
-0.10	0.00	0.000	-0.3540
		0.005	-0.3465
		0.010	-0.3395
-0.30	0.00	0.000	-0.2383
		0.005	-0.2305
		0.010	-0.2231
-0.30	0.20	0.000	-0.3488
		0.005	-0.3408
		0.010	-0.3332

Table 3.1: Binding energies of the twenty-site cluster as a function of t', t'', and $\delta t'$

While the strength of the binding is weakened by the anisotropy, the effect is quite small, and bound pairs are still the most favourable behaviour of the charge carriers. Note that while the energy changes are small, the introduction of anisotropy can have a much more decided effect by changing the ground state wave vector of the model. If an excited state with similar energy to the ground state is favoured by the introduction of anisotropy, it is possible for this excited state to become the new ground state. Given that the new ground state can have much different symmetry than the old, this can have a profound effect on other measurable quantities. This possibility will be discussed in further sections.

3.3 Magnetic Properties

As discussed in section 1.3, the magnetic properties of the cuprates provide the primary signatures for stripes. The stripe phase is characterised by the formation of spin waves, and static magnetic peaks which are IC with the lattice. These quantities can be examined within the model with the use of the SSCF, and $S(\vec{q})$, respectively.

The SSCF [23] is defined as

$$C_{ss}(\vec{r}) = \frac{1}{N_T} \sum_i \left\langle E_0^N \left| \mathbf{S}_i \cdot \mathbf{S}_{i+\vec{r}} \right| E_0^N \right\rangle. \tag{3.2}$$

This function measures the averaged spin orientation as a function of distance. The values given for a specific $\vec{r}$ value correspond to the probability of that site containing an electron, with positive values indicating same spin, and negative values indicating opposite spin. The results for the $t - J$ model at low doping should show alternating positive and negative values as $\vec{r}$ is increased by a lattice spacing, with the absolute value of the results diminishing as $\vec{r}$ is increased. This result is indicative of strong short-range AF behaviour, an important property of the cuprates. As the doping level is increased, the magnetic correlations diminish, as one would expect since fewer electrons are present. All of the values for this function presented in this work are multiplied by a staggering term $(-1)^{r_x + r_y}$. This term makes all the values positive if they are antiferromagnetically aligned, while negative values indicate alignment of spin not consistent with antiferromagnetism. This makes the presence of antiferromagnetism much clearer in the results.

In figure 3.2, the results found for this quantity are shown, for a cluster of twenty sites with one hole and $J = 0.4t$. The results show the strong antiferromagnetism previously discussed, with all spins within the cluster being antiferromagnetically aligned. This tendency is affected very little by the parameters. As t' is decreased from $t' = 0t$ to $t' = -0.3t$, the long-range correlations appear to strengthen, while the

t'=-0.10 t"=0.00

```
        0.1250   0.1200   0.1233
        0.1537   0.2601   0.1362   0.1167
0.1348  0.2930  [0.7125]  0.2930   0.1348
0.1167  0.1362   0.2601   0.1537   0.1508
        0.1200   0.1250
        0.0993
```

t'=-0.09/-0.11 t"=0.00

```
        0.1255   0.1203   0.1236
        0.1543   0.2606   0.1367   0.1171
0.1351  0.2930  [0.7125]  0.2930   0.1351
0.1171  0.1367   0.2606   0.1543   0.1515
        0.1203   0.1255
        0.0998
```

t'=-0.30 t"=0.00

```
        0.1410   0.1302   0.1323
        0.1641   0.2903   0.1408   0.1293
0.1347  0.2605  [0.7125]  0.2605   0.1347
0.1293  0.1408   0.2903   0.1641   0.1642
        0.1302   0.1410
        0.1242
```

t'=-0.29/-0.31 t"=0.00

```
        0.1416   0.1306   0.1324
        0.1648   0.2910   0.1410   0.1296
0.1350  0.2606  [0.7125]  0.2606   0.1350
0.1296  0.1410   0.2910   0.1648   0.1643
        0.1306   0.1416
        0.1245
```

t'=-0.30 t"=0.20

```
        0.1316   0.1247   0.1230
        0.1571   0.2909   0.1342   0.1189
0.1264  0.2581  [0.7125]  0.2581   0.1264
0.1189  0.1342   0.2909   0.1571   0.1571
        0.1247   0.1316
        0.1193
```

t'=-0.29/-0.31 t"=0.20

```
        0.1324   0.1252   0.1232
        0.1578   0.2917   0.1344   0.1192
0.1269  0.2581  [0.7125]  0.2581   0.1269
0.1192  0.1344   0.2917   0.1578   0.1575
        0.1252   0.1324
        0.1197
```

Figure 3.2: The staggered SSCF for the twenty-site cluster with one hole. The boxed numbers denote $\vec{r} = (0,0)$. The extended parameters used are shown above each case, with $J = 0.4t$ for all cases. The results on the left are for the isotropic case for the parameters shown, while the results on the right are anisotropic with $\delta t = 0.01t$.

nearest neighbour correlations remain at the same values. However, the symmetry of the nearest neighbour correlations is rotated by 90°. This is most likely due to a change in the ground state symmetry of the problem, since the one hole ground state wave vector is altered from $\vec{k} = (3\pi/5, 2\pi/5)$ to $\vec{k} = (\pi/5, 2\pi/5)$ with this change in t'. The t'' term appears to act as a dampening effect on t', causing most values to revert to values closer to the $t' = 0t$ case. When the anisotropy is introduced, very little change occurs. Figure 3.2 shows the values for the SSCF when $\delta t = 0.01t$, the extreme anisotropy limit. The values do not change by any appreciable amount. The greatest change is approximately 0.008 in magnitude, which is less than 10% of

the lowest value. The symmetry seems to be dominated by the wave vector, and the small change in symmetry caused by the introduction of the anisotropy does little to change this.

The results for the SSCF for the twenty-site cluster with two holes are presented in figure 3.3. The left-hand side of the diagram illustrates the isotropic results for the three different sets of parameters. As in the one hole case, the spins show AF behaviour at short range, which diminishes as $\vec{r}$ increases. At the edges of the cluster, the values become slightly negative, indicating that the orientation of the spins does not follow the AF pattern with respect to the central spin. All the values are isotropic in this case, due to the $\pi/4$ rotational symmetry of the two-hole ground state. The values are not affected greatly by the differing parameters. The changes induced by the introduction of extreme (10%) anisotropy can be seen on the right side of figure 3.3. The changes are much greater than those seen in the one hole case, which could be attributed to the change in the ground state symmetry.

The LTO phase causes a preferred direction to appear, yet the sum of the values at a given $\vec{r}$ value remains the same in both phases. The SSCF is therefore conserved through the change, while the values are "split" between the two directions. The splitting of the values is most prominent at $\sqrt{5}a$, with a similarly strong split at $\sqrt{2}a$. The $\sqrt{5}a$ sites are not equivalent and show a clear difference in the change of the magnitude. Two of the $\sqrt{5}a$ sites have the correct AF sign and the other four have the opposite sign. The motion of the two holes in the LTO phase is less disruptive to the spin background in the (1, -1) direction, while it is more disruptive to the spin ordering in the (1, 1) direction. The cluster is too small to say for sure, but it appears as though AF stripes are being formed along the (2, -1) direction that have a modulation in the (1, 2) direction. It should be noted that on the twenty-site cluster, the $\sqrt{8}a$ sites are the $2a$ sites because of the periodic boundary conditions. Thus, even though a spin modulation wave appears to occur, the precise direction is unclear

t'=-0.10 t"=0.00

```
                  -0.0083   0.0101   0.0567
          0.0695   0.2185   0.0695  -0.0083
  0.0101   0.2185  [0.6750]  0.2185   0.0101
 -0.0083   0.0695   0.2185   0.0695   0.0567
          0.0101  -0.0083
                  -0.0394
```

t'=-0.09/-0.11 t"=0.00

```
                  -0.0056   0.0039   0.0431
          0.0769   0.2105   0.0620  -0.0112
  0.0164   0.2263  [0.6750]  0.2263   0.0164
 -0.0112   0.0620   0.2105   0.0769   0.0705
          0.0039  -0.0056
                  -0.0397
```

t'=-0.30 t"=0.00

```
                  -0.0114   0.0017   0.0654
          0.0674   0.2069   0.0674  -0.0114
  0.0017   0.2069  [0.6750]  0.2069   0.0017
 -0.0114   0.0674   0.2069   0.0674   0.0654
          0.0017  -0.0114
                  -0.0387
```

t'=-0.29/-0.31 t"=0.00

```
                  -0.0089  -0.0042   0.0511
          0.0601   0.2002   0.0601  -0.0141
  0.0077   0.2136  [0.6750]  0.2136   0.0077
 -0.0141   0.0601   0.2002   0.0747   0.0798
         -0.0042  -0.0089
                  -0.0390
```

t'=-0.30 t"=0.20

```
                  -0.0160   0.0009   0.0542
          0.0661   0.2127   0.0661  -0.0160
  0.0009   0.2127  [0.6750]  0.2127   0.0009
 -0.0160   0.0661   0.2127   0.0661   0.0542
          0.0009  -0.0160
                  -0.0479
```

t'=-0.29/-0.31 t"=0.20

```
                  -0.0191  -0.0108   0.0418
          0.0693   0.2027   0.0572  -0.0239
  0.0000   0.2134  [0.6750]  0.2134   0.0000
 -0.0239   0.0572   0.2027   0.0693   0.0655
         -0.0108  -0.0191
                  -0.0531
```
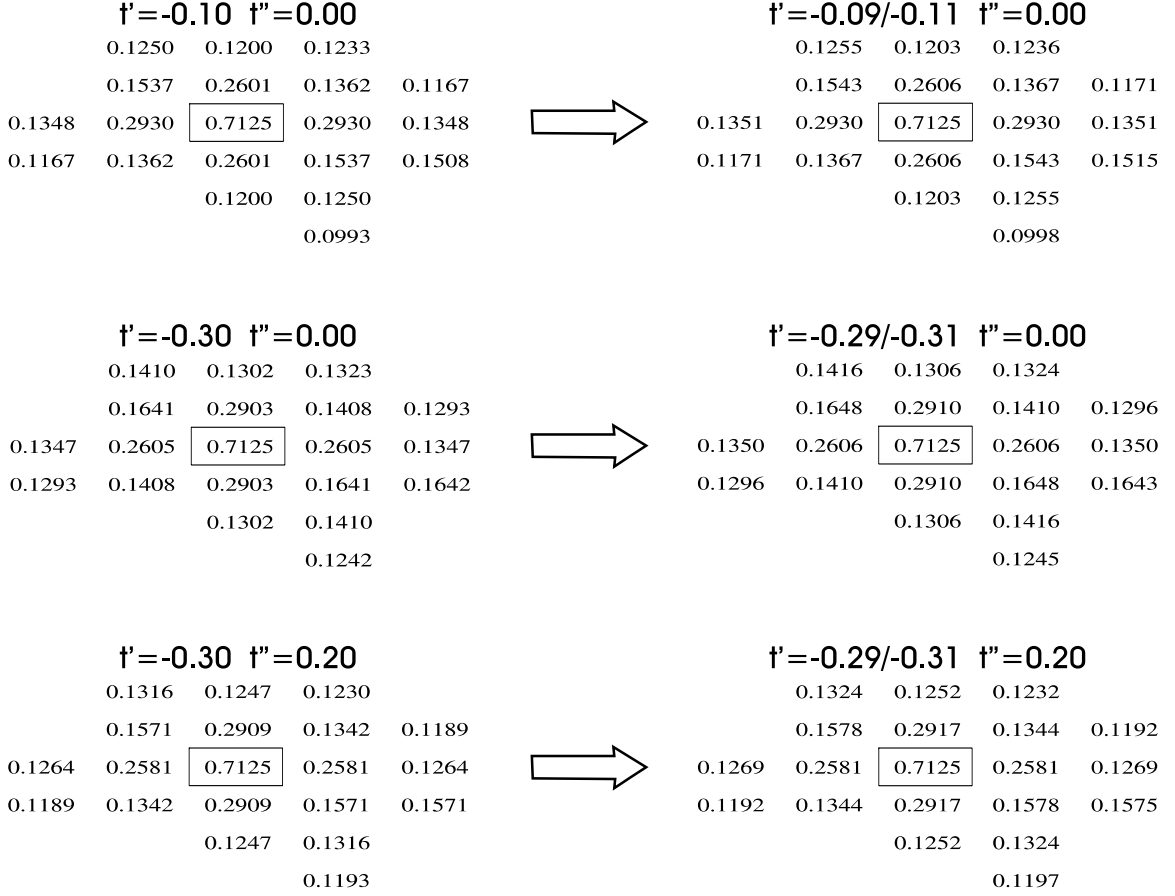
Figure 3.3: The staggered SSCF for the twenty-site cluster with two holes. The boxed numbers denote $\vec{r} = (0,0)$. Negative results are printed in red, for clarity. The extended parameters used are printed above each case, with $J = 0.4t$ for all cases. The results on the left are for the isotropic case for the parameters shown, while the results on the right are anisotropic with $\delta t = 0.01t$.

because these sites are identical for this cluster.

The static magnetic structure factor $S(\vec{q})$, defined as

$$S(\vec{q}) = \sum_{\vec{r}} e^{i\vec{q}\cdot\vec{r}} C_{ss}(\vec{r}), \tag{3.3}$$

is another measure of the magnetic configuration of the lattice. While the SSCF measures spin correlations in real space, $S(\vec{q})$ measures these correlations in reciprocal space. The AF tendency of the model can be seen in the (π, π) peak, the strength

of which is indicative of the strength of the short-range magnetic correlations measured by the SSCF. The advantage of this function over the SSCF is that real-space measurements are difficult to evaluate experimentally. The static magnetic structure factor $S(\vec{q})$, however, can easily be found experimentally using neutron scattering.

The primary reason to examine this quantity is to probe the existence of IC magnetic peaks. The AF (π, π) peak discussed above is split into four distinct peaks in the neutron scattering data of Tranquada *et al.* [22]. In the *t-J* model, this can be seen by the reduction of weight in the (π, π) peak of $S(\vec{q})$, and the increase in weight of this quantity at values closest to this peak. This is generally difficult within the confines of the small clusters available to the ED method, as discussed in section 2.5.1. The closest wave vectors within the twenty-site cluster lie at the $\vec{k} = (\frac{4\pi}{5}, \frac{3\pi}{5})$ point, and all rotations of this point.

Table 3.2 shows the numerical values obtained for $S(\vec{q})$ for the reciprocal lattice vectors (π, π), $(4\pi/5, 3\pi/5)$, and $(3\pi/5, -4\pi/5)$ in the LTO phase for the undoped, one-hole, and two-hole cases. This table illustrates the rapid decrease of $S(\pi, \pi)$ as a function of doping, and similarly the rapid increase of $S(4\pi/5, 3\pi/5)$ and $S(3\pi/5, -4\pi/5)$ with doping. These results are consistent with the formation of IC peaks around (π, π), although the lack of wave vectors around (π, π) for this particular cluster prevents conclusive evidence of this. When the system is doped with one hole, the anisotropy enhances $S(\pi, \pi)$ in agreement with the experimental results, which observed no IC peak at very low doping. The IC peaks start to form at a larger doping concentration, which is in agreement with our results when the doping is increased from one hole to two holes. The results for the anisotropic case are also presented in table 3.2. This phase shows similar behavior, but note that the symmetry evident here in the two-hole state is lost in this case at the same level of doping. The difference between the phases is very small in the one hole case, but becomes larger in the two-hole case. The values $S(4\pi/5, 3\pi/5)$ and $S(3\pi/5, -4\pi/5)$

$\vec{q} =$	$\vec{q_1}$		$\vec{q_2}$		$\vec{q_3}$	
$|\delta t'|\backslash$ holes	1	2	1	2	1	2
(-0.1; 0.0)						
0.000	3.6180	1.9079	1.0894	1.2809	0.9016	1.2809
0.010	3.6225	1.9078	1.0895	1.3155	0.9011	1.2465
0.020	3.6269	1.9073	1.0896	1.3498	0.9005	1.2127
(-0.3; 0.0)						
0.000	3.7570	1.8252	0.9793	1.2676	0.8743	1.2676
0.010	3.7611	1.8252	0.9792	1.3017	0.8737	1.2337
0.020	3.7650	1.8252	0.9792	1.3354	0.8732	1.2003
(-0.3; 0.2)						
0.000	3.5818	1.7068	1.0225	1.3098	0.9118	1.3098
0.010	3.5871	1.7068	1.0222	1.3384	0.9109	1.2812
0.020	3.5923	1.7068	1.0220	1.3670	0.9100	1.2530

Table 3.2: $S(\vec{q})$ as a function of doping, the anisotropy, and the parameters. The three wavevectors are; $\vec{q_1} = (\pi, \pi)$, $\vec{q_2} = (4\pi/5, 3\pi/5)$, and $\vec{q_3} = (3\pi/5, -4\pi/5)$. The three respective values for the undoped cluster are; 5.1546, 0.9222, and 0.9222.

in the anisotropic case exhibit a percentage change of $+6.1\%$ and -6.9% relative to the isotropic case. The percentage difference between the two is proportional to $\delta t'$. The nonsymmetrical growth of the values for $S(4\pi/5, 3\pi/5)$ and $S(3\pi/5, -4\pi/5)$ as a function of doping seems to indicate unidirectional IC peaks in agreement with the experimental results obtained by Wakimoto *et al.* [28] and by Fujita *et al.* [72] at x = 0.05.

3.4   Charge Ordering

Given that the changes in the one hole case are fairly small, as shown in the previous section, it is worthwhile to examine the relationships between the holes in the two-hole case and what effects the anisotropy has on the two-hole state. While indeed this may be outside the low doping regime for small clusters such as the twenty-site cluster, the effect may well be based simply on the absolute number of holes rather than the relative concentration. Therefore larger clusters could exhibit similar results

while still being in the appropriate doping regime.

In order to study the real-space distribution of the holes, the HHCF defined in equation 2.7 will be used. This function gives the numerical probability values for hole placement as a function of distance. This probability is relative, and is indicative of the hole spacing rather than the absolute placement of the holes within the cluster. Previous measurements for this quantity within the $t - J$ model have shown that two holes prefer to form a bound pair with a separation of $\sqrt{2}a$ [73, 50, 51, 70]. This distribution is energetically favourable since the frustration to the spin background caused by the holes is reduced. When additional hopping terms are included, as in the extended $t - J$ model, the holes separate as the kinetic energy of the holes is increased. These results show a competition between the magnetic and kinetic energies of the system. The magnetic energy is minimised by having the two holes on opposite sublattices so that the magnetic frustration to the lattice is reduced, and on nearest neighbour sites to reduce the number of missing bonds. Having two holes on the same sublattice of the model, say two lattice spacings apart, would cause more AF bonds to be broken. The kinetic energy of the holes is minimised by spacing the holes far apart, as this allows motion of the holes to be free. A compromise between these two factors is to have the holes spaced at distances of $3a$ or $\sqrt{5}a$. This agrees with the results presented in figure 3.4. In the case where $t' = -0.1t$, the maximum in the HHCF occurs at $\sqrt{2}a$, which is in agreement with the previous results for the $t - J$ model [73, 50, 51, 70]. This is justified by the low kinetic energy present. As t' is decreased below $-0.1t$, the maximum shifts to $\sqrt{5}a$. The inclusion of a positive t'' shifts a significant amount of the weight from the inner sites to the outer sites so that $\sqrt{10}a$ is the maximum for the parameters $t' = -0.2t$ and $t'' = 0.1t$. Figure 3.4 shows the same maximum at a distance of $\sqrt{10}a$ for the parameters $t' = -0.3t$ and $t'' = 0.2t$. Note that even though the holes are as far apart as possible, they are still bound together according to the binding energy results discussed in the previous

t'=-0.10 t"=0.00

```
        0.0556    0.0478    0.0616
        0.0622    0.0388    0.0622    0.0556
0.0478  0.0388    XXXX      0.0388    0.0478
0.0556  0.0622    0.0388    0.0622    0.0616
        0.0478    0.0556
        0.0590
```

t'=-0.09/-0.11 t"=0.00

```
        0.0573    0.0460    0.0567
        0.0655    0.0380    0.0588    0.0540
0.0498  0.0395    XXXX      0.0395    0.0498
0.0540  0.0588    0.0380    0.0655    0.0666
        0.0460    0.0573
        0.0590
```

t'=-0.30 t"=0.00

```
        0.0579    0.0522    0.0663
        0.0574    0.0339    0.0574    0.0579
0.0522  0.0339    XXXX      0.0339    0.0522
0.0579  0.0574    0.0339    0.0574    0.0663
        0.0522    0.0579
        0.0619
```

t'=-0.29/-0.31 t"=0.00

```
        0.0596    0.0497    0.0608
        0.0608    0.0328    0.0539    0.0562
0.0548  0.0348    XXXX      0.0348    0.0548
0.0562  0.0539    0.0328    0.0608    0.0719
        0.0497    0.0596
        0.0619
```

t'=-0.30 t"=0.20

```
        0.0573    0.0498    0.0635
        0.0591    0.0361    0.0591    0.0573
0.0498  0.0361    XXXX      0.0361    0.0498
0.0573  0.0591    0.0361    0.0591    0.0635
        0.0498    0.0573
                  0.0639
```

t'=-0.29/-0.31 t"=0.20

```
        0.0588    0.0480    0.0591
        0.0619    0.0352    0.0561    0.0558
0.0518  0.0369    XXXX      0.0369    0.0518
0.0558  0.0561    0.0352    0.0619    0.0679
        0.0480    0.0588
        0.0640
```
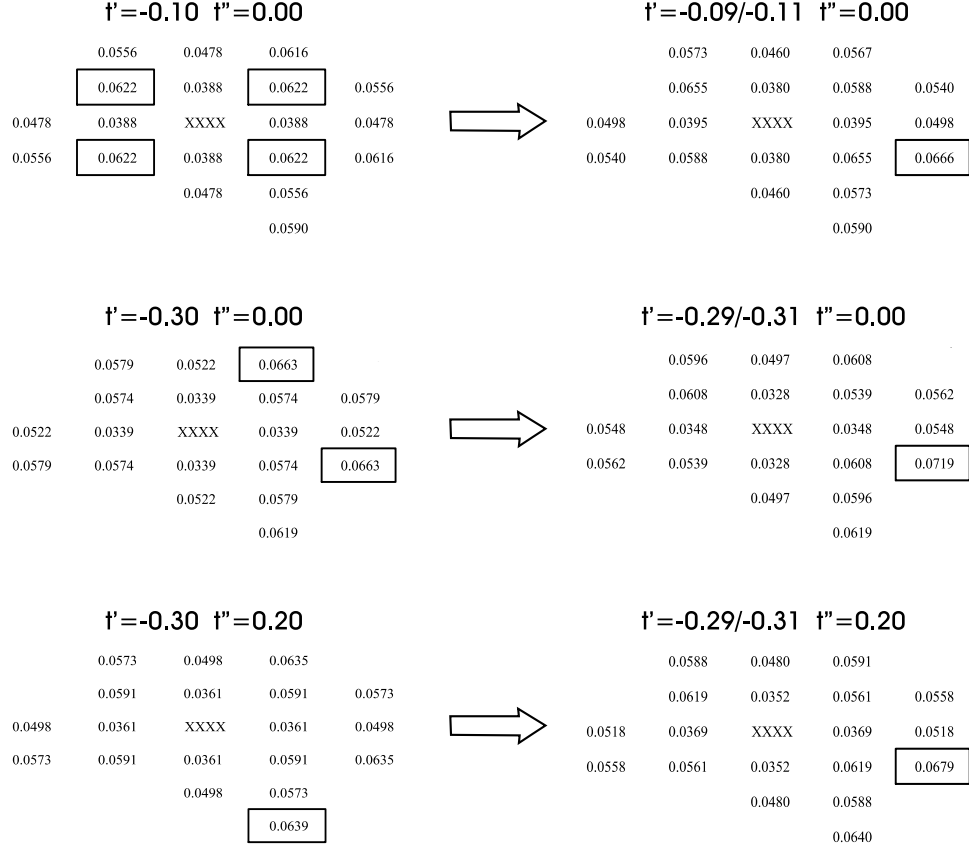
Figure 3.4: Isotropic and anisotropic results for the HHCF for the twenty-site cluster with two holes. The parameters used are printed above each case, with $J = 0.4t$. The XXXX denotes the location of the first hole. The boxed number is the highest probability of finding the second hole. The results on the left are for the isotropic case for the parameters shown, while the results on the right are for the anisotropic case with $\delta t = 0.01t$.

section.

The introduction of an anisotropic t' produces some interesting behavior, as can be seen in the results on the right side of figure 3.4. The HHCF at the $\sqrt{10}a$ site does not change as the anisotropy is increased. To a lesser degree, there is not much change at the nearest neighbor sites $(\pm a, 0)$ and $(0, \pm a)$ either. The majority of the change is at the $\sqrt{2}a$ and $\sqrt{5}a$ sites. Regardless of the values of t' and t'', the second hole prefers to lie at site 8 in figure 3.1, which corresponds to a distance of $\sqrt{5}a$. The placement of the holes at these locations results in a half-filled charge carrier stripe at
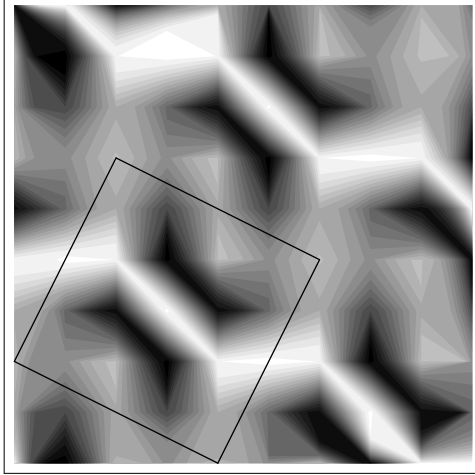
Figure 3.5: Graphical representation of the placement of holes within the twenty-site cluster with two holes, in the LTO phase. The whiter the area, the greater the probability of hole placement. The parameters used are $J = 0.40t$, $t' = -0.09t/ - 0.11t$, and $t'' = 0.00t$. The cluster is shown in a ten site by ten site array by using periodic boundary conditions. The boundaries of one cluster are shown for clarity.

an orientation of $\sim -25^o$ due to the periodic boundary conditions. This is illustrated graphically in figure 3.5.

The notion that the holes are forming bounded one-dimensional stripes in the LTO phase is supported by the binding energies given in Table 3.1. Although for each parameter set the binding energy is decreased in magnitude as the level of anisotropy increases, the magnitude of the change is quite small. Thus, regardless of the parameter set used, implementation of an anisotropic t' into this model results in the formation of half-filled, bounded, charge carrier stripes. The only effect that the parameters have lie in the level of anisotropy required to produce this phase. For the case where $t'_{x+y} = -0.09t$, $t'_{x-y} = -0.11t$, an anisotropy of $\delta t' = 0.008t$ is required to shift the maximum from the $\sqrt{2}a$ sites in the isotropic case to the $\sqrt{5}a$ distance. An anisotropy of only $\delta t' = 0.002t$ is required in the $t'_{x+y} = -0.29t$, $t'_{x-y} = -0.31t$, $t'' = 0.20t$ case to shift the maximum from the $\sqrt{10}a$ site in the isotropic case to the $\sqrt{5}a$ distance in the anisotropic case.

The anisotropy in the HHCF is most robust at the four sites of distance $\sqrt{2}a$

and the six sites of distance $\sqrt{5}a$ with a percentage change on the order of $\delta t'$. The emergence of a preferred direction is well supported, with values in the second and fourth quadrants being higher than the corresponding distances in the first and third quadrants. In an attempt to quantify the change, we can examine the percentage difference of the HHCF, defined as

$$\Delta C_{hh}(\vec{r}_1, \vec{r}_2) = 200 \left| \frac{C_{hh}(\vec{r}_1) - C_{hh}(\vec{r}_2)}{C_{hh}(\vec{r}_1) + C_{hh}(\vec{r}_2)} \right|. \tag{3.4}$$

$\Delta C_{hh}(\vec{r}_1, \vec{r}_2)$ is plotted in figure 3.6 as a function of $\delta t'$ and clearly shows the linear relationship between the two. It is worth noting that $\Delta C_{hh}(\vec{r}_1, \vec{r}_2)$ depends linearly on the difference in t' and not on the percentage change in t'. These results illustrate the split in the HHCF between the quadrants. It turns out that the percentage difference in the HHCF is independent of the specific values of t' and of t'', and only depends on $\delta t'$. This independence is only to leading order of magnitude since the values of t' and t'' will play a role with a large anisotropy.

3.5 Dynamic Magnetic Properties

The properties of transitions between magnetic states can be evaluated using the dynamic magnetic structure factor $S^\mu(\vec{q}, \omega)$ [23]. This function differs from its static counterpart in its frequency dependence, and is defined as

$$S^\mu(\vec{q}, \omega) = \langle E_0^N | S^{\mu\dagger}(\vec{q}) \frac{1}{z - H} S^\mu(\vec{q}) | E_0^N \rangle, \; (\mu = +, -, z), \tag{3.5}$$

where $z = \omega + i\epsilon + E_0$. Transitions between states of differing spin number S can be evaluated using $\mu = +, -$. Evaluation of this quantity results in an absorption spectrum, the peaks of which correspond to the energy of the excitations. The existence of a spin gap can be ascertained from this spectrum by noting the location of the first peak, which indicates the first available spin excitation. Note that in the
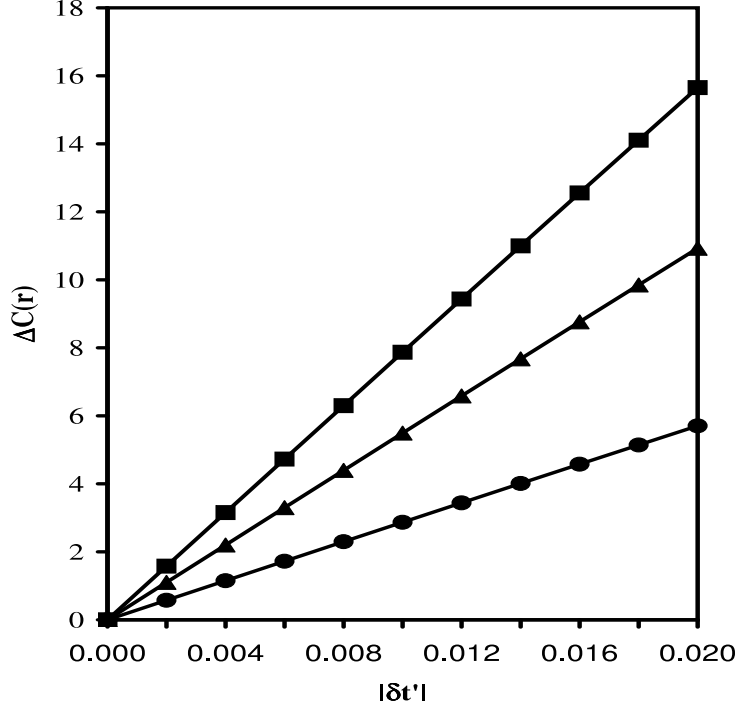
Figure 3.6: The percentage difference in the HHCF as a function of the difference in t' for the parameters $(t', t'') = (-0.3, 0.2)$. The first hole is located at site 11 in figure 3.1. The squares are for $|\vec{r}| = \sqrt{5}a$ (sites 1 and 14), the triangles are for $|\vec{r}| = \sqrt{2}a$ (sites 8 and 17), and the circles are for $|\vec{r}| = \sqrt{5}a$ (sites 3 and 18). A detailed definition of the percentage difference can be found in the text.

absence of an external magnetic field, the components S^z, S^x, and S^y of the total spin $\vec{S}$ are equal. Given that $S^x = \frac{1}{2}(S^+ + S^-)$, it is sufficient to calculate only S^z in the $S = 0$ state. In this state the $S^{+,-}$ operators are equivalent, and will therefore each contribute half of the weight of the S^x spectrum. Note that the weight of the spectrum provided by $S(\vec{q}, \omega)$ is directly related to $S(\vec{q})$, with $\int S(\vec{q}, \omega) d\omega = S(\vec{q})$.

Previous results for this function [74, 75] within the $t - J$ model have focussed on the S^z results, at the AF wave vector $\vec{Q} = (\pi, \pi)$. These results show the existence of a large low energy peak at $\vec{q} = (\pi, \pi)$ for $x < 0.25$, which diminishes and nearly vanishes at higher doping concentrations. This is consistent with the static magnetic results. Studies of this quantity typically examine $S = 0$ states, which are able to
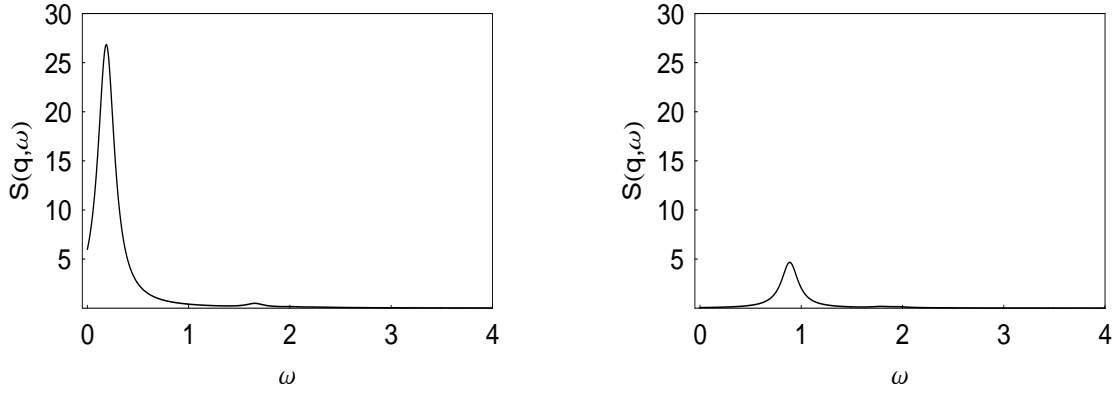
Figure 3.7: $S^z(\vec{q}, \omega)$ results for the twenty-site cluster with zero holes in the isotropic case. The figure on the left is for $\vec{q} = (\pi, \pi)$, the right for $\vec{q} = (4\pi/5, 3\pi/5)$. $J = 0.4t$ for both figures. The units for the y-axis are arbitrary, while ω is in units of t.

reproduce the predominantly AF behaviour seen in the cuprates.

In order to view the effects of doping on $S^z(\vec{q}, \omega)$, results from zero- and two-hole cases in the twenty-site cluster will be presented. The one-hole cases have been omitted, since these do not represent an $S = 0$ state. The zero-hole results for $S^z(\vec{q}, \omega)$ are presented in figure 3.7, for $\vec{q} = (\pi, \pi)$ and $\vec{q} = (4\pi/5, 3\pi/5)$. The latter wave vector is the closest to the (π, π) point within this cluster, so any evidence of IC peaks would most likely be seen here. The results for both wave vectors show a single excitation peak, with no feature elsewhere in the spectrum. The peak for $\vec{q} = (\pi, \pi)$ is quite large, with a magnitude approximately 5.7 times that of the $\vec{q} = (4\pi/5, 3\pi/5)$ peak. The $\vec{q} = (4\pi/5, 3\pi/5)$ peak is also shifted to much higher energy, with the peak at this wave vector occurring at $\omega = 0.89t$ as opposed to $\omega = 0.19t$ for the $\vec{q} = (\pi, \pi)$ peak.

The two-hole results for $S^z(\vec{q}, \omega)$ in the twenty-site cluster for $\vec{q} = (\pi, \pi)$ and $\vec{q} = (4\pi/5, 3\pi/5)$ are presented in figure 3.8, for two different parameter sets. The existence of the large low energy peak at $\vec{q} = (\pi, \pi)$ can still be seen, although the magnitude is diminished somewhat from the zero-hole case. This peak is centered at $\omega = 0.35t$ with a magnitude of 9.8719 for the $t' = -0.10t$ case, while the peak
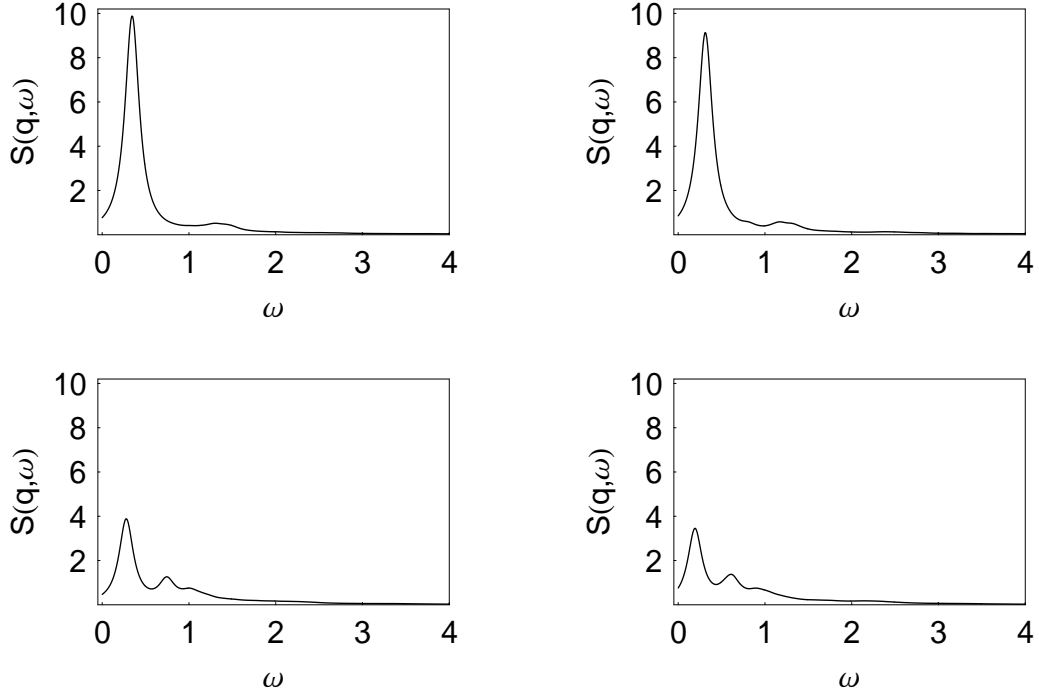
Figure 3.8: $S^z(\vec{q}, \omega)$ results for the twenty-site cluster with two holes in the isotropic case. The figures on the top and bottom are for $\vec{q} = (\pi, \pi)$ and $\vec{q} = (4\pi/5, 3\pi/5)$, respectively, while the figures on the left and right are for $t' = -0.10t$ and $t' = -0.30t$, respectively. $J = 0.4t$ and $t'' = 0$ for all the results. The units for the y-axis are arbitrary, while ω is in units of t.

is centered at $\omega = 0.31t$ with a magnitude of 9.1354 for the $t' = -0.30t$ case. The intensity of this first excitation peak is roughly 40% of that of the zero-hole case, for both parameter sets. Note that this is approximately the same level of reduction seen in $S(\pi, \pi)$ when comparing the undoped case to the two-hole case. These results agree with those seen in the previous studies of this quantity [74]. The results for the $\vec{q} = (4\pi/5, 3\pi/5)$ wave vector show a smaller peak than the $\vec{q} = (\pi, \pi)$ spectrum, but the difference is less pronounced than in the zero-hole case. Note here the existence of three peaks as opposed to the one primary peak of the $\vec{q} = (\pi, \pi)$ spectrum. The first peak in the $\vec{q} = (4\pi/5, 3\pi/5)$ case is centered at $\omega = 0.28t$ with a magnitude of 3.8874 for the $t' = -0.10t$ case, while it is centered at $\omega = 0.19t$ with a magnitude
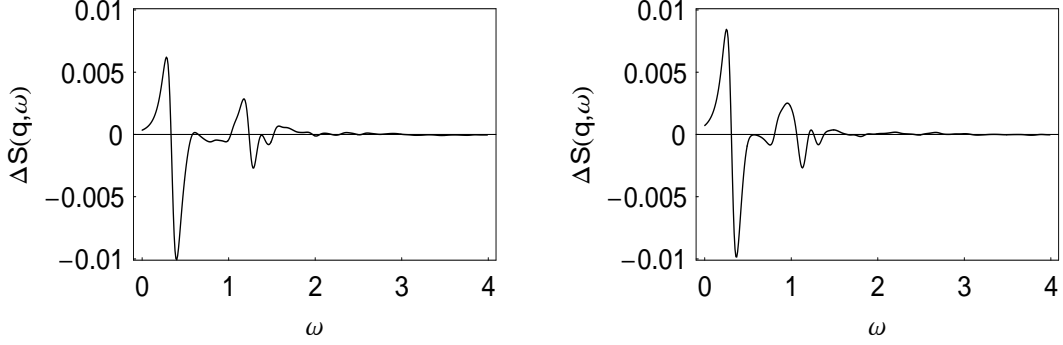
Figure 3.9: $\Delta S^z(\vec{q}, \omega)$ results for the twenty-site cluster with two holes, for $q = (\pi, \pi)$. The figure on the left is for $t' = -0.10t$, the right for $t' = -0.30t$.

of 3.4540 for the $t' = -0.30t$ case. The isotropic results show a similar response to the parameter values for both wave vectors, with the $t' = -0.10t$ case having a larger first excitation peak at higher energy than the $t' = -0.30t$ case.

Upon introduction of $\delta t = 0.10$, the spectra show changes similar to those seen in $S(\vec{q})$. For $\vec{q} = (\pi, \pi)$, the location of the low energy peak shifts very slightly to $\omega = 0.35t$ from $\omega = 0.34t$ for the $t' = -0.10t$ case, while the peak for the $t' = -0.30t$ case remains at $\omega = 0.31t$. The magnitude of the peak is relatively unchanged, which agrees with the $S(\vec{q})$ results. To illustrate the difference between the isotropic and anisotropic spectra, we shall define a quantity $\Delta S^z(\vec{q}, \omega) = S^z_{aniso}(\vec{q}, \omega) - S^z_{iso}(\vec{q}, \omega)$. Figure 3.9 shows $\Delta S^z(\vec{q}, \omega)$ as a function of ω for both parameter sets used. The results are very similar in both cases, with two shifts in peaks being shown for each parameter set. These shifts are indicated by the portions of the graphs where $\Delta S^z(\vec{q}, \omega)$ makes a transition from positive to negative values, which would correspond to a shift to lower ω. Note that the largest magnitude of $\Delta S^z(\vec{q}, \omega)$ is roughly 0.01, which is only 0.1% of the maximum isotropic value. Thus even though a reduction in the spin gap is seen for both parameter sets, the difference is so minimal that it can essentially be ignored for this wave vector.

The $\vec{q} = (4\pi/5, 3\pi/5)$ and $\vec{q} = (3\pi/5, -4\pi/5)$ results for $\Delta S^z(\vec{q}, \omega)$ are shown in
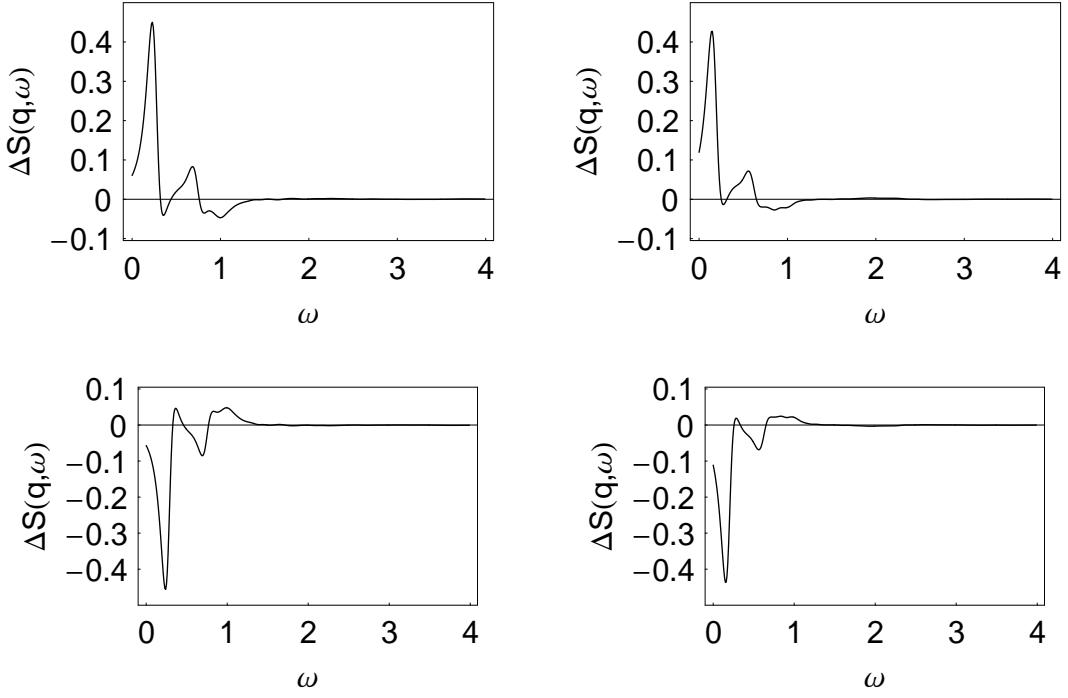
48

Figure 3.10: $\Delta S^z(\vec{q}, \omega)$ results for the twenty-site cluster with two holes. The top and bottom figures are for $q = (4\pi/5, 3\pi/5)$ and $q = (3\pi/5, -4\pi/5)$, respectively, while the figures on the left and right are for $t' = -0.10t$ and $t' = -0.30t$, respectively.

figure 3.10. These results illustrate a considerably larger degree of change for this wave vector, as opposed to $\vec{q} = (\pi, \pi)$. The highest magnitude of change is 0.4265 for the $t' = -0.30$ case and 0.4501 for the $t' = -0.10$ case, which are approximately 12% of the peak values seen in the isotropic case. The values also appear shifted to lower ω in both parameter sets. The prevalence of positive data for this function indicates that the anisotropic case has higher values throughout most of the spectrum, representing an overall increase of the weight of $S(\vec{q}, \omega)$ upon introduction of the anisotropic parameters. The increase in weight for this wave vector is offset by the decrease in weight at the wave vector $\vec{q} = (3\pi/5, -4\pi/5)$, which is the $\vec{q} = (4\pi/5, 3\pi/5)$ vector rotated by $\pi/2$. The spectra shown are almost identical in shape, but mirrored over the x-axis. This would indicate that the magnitude of the change is the same in both

cases, but the $\vec{q} = (3\pi/5, -4\pi/5)$ results have been shifted to higher ω as opposed to lower ω.

The splitting of the weight between the $\vec{q} = (4\pi/5, 3\pi/5)$ and $\vec{q} = (3\pi/5, -4\pi/5)$ results is also seen in the $S(\vec{q})$ results seen in the previous section. This is not surprising considering the relation between the two functions. However, the $S(\vec{q}, \omega)$ results illustrate the splitting of the position of the peak, in addition to the magnitude. This indicates that the spin excitation is of lower energy in one direction than the other, and thus represents a preferred direction for a spin modulation. From the results shown in this section, it appears as though this spin modulation is forming along the $\vec{q} = (4\pi/5, 3\pi/5)$ direction, which is rotated by almost 90° from the direction of the charge stripe.

3.6   Summary

The chapter focussed on the examination of the LTO phase in the low doping regime of $La_{2-x}Sr_xCuO_4$. This examination was carried out on a twenty-site cluster by using a variety of correlation functions. Similar results were found for most of the functions presented. The SSCF and $S(\vec{q})$ results show strong AF behaviour for both the one- and two-hole cases. The anisotropy had little effect on the one-hole case, while a much more pronounced effect is seen in the two-hole case. A spin modulation seems to appear in the two-hole case, but the precise direction is unclear. The HHCF results in the isotropic case show a different preferred configuration for each parameter set. Upon introduction of anisotropy, the holes align in a state where they are all at a distance of $\sqrt{5}a$ apart, regardless of the parameters. This state appears as a stripe when the periodic boundary conditions are considered. The existence of a "split" of the correlation functions between the $\hat{x} + \hat{y}$ and $\hat{x} - \hat{y}$ directions can be seen in the HHCF and SSCF, as well as in $S(\vec{q})$. This "splitting" is conserved, that is to say, the increase in weight in one direction is equal to the decrease in weight in the

other. When the magnitude of the split in the HHCF is graphed versus the level of anisotropy, a perfectly linear relationship is found. This splitting is also seen in the results for $S(\vec{q}, \omega)$, which show a shift in the peak positions for $\vec{q} = (4\pi/5, 3\pi/5)$ and $\vec{q} = (3\pi/5, -4\pi/5)$, in addition to a splitting of the weight.

Chapter 4

LTT Phase

4.1 Introduction

The experiments by Tranquada *et al.* [22] on $La_{1.6-x}Sr_xNd_{0.4}CuO_4$ revealed the existence of a static stripe phase for $x = 0.125$, which was thought to be responsible for the suppression of the superconducting state at this level of doping. The reason for the appearance of stripes in this compound as opposed to the lack of stripes in $La_{2-x}Sr_xCuO_4$ was attributed to the structural change of the compound from the LTO phase to the LTT phase when Nd ions are doped into the lattice. The LTT phase, shown in figure 1.6, shows the structural change caused by the Nd ions. The buckling of the planes causes the on-plane Cu-O-Cu bonds to become anisotropic. Since these bonds are the nearest neighbour bonds in the *t-J* model, the nearest neighbour parameters t and J should reflect this anisotropy if this compound is to be analysed correctly.

4.2 Parameters

The buckling of the CuO_2 planes caused by the LTO $\rightarrow$ LTT transition results in a change in the bond angle of the copper-oxygen in-plane bonds. The separation between the ions remains mostly unchanged, but the orbital overlap between the copper and oxygen ions is affected by the change in angle. Since the hopping parameter t within the $t - J$ model is based on this overlap, an anisotropy in t would be expected.

Normand and Kampf [76] estimated the angular dependancy of t as

$$t_y = t_x \mid cos(\pi - 2\Phi) \mid, \tag{4.1}$$

where Φ is the bond angle. Investigation of the bond angle within the compound has revealed the distortion to be not more than 5°, which results in the percentage difference between t_x and t_y, $\mid t_x - t_y \mid /t_x$, to be approximately 1.5%. Given that $J \propto t^2$ within the model (see Appendix A), this would create an anisotropy in J of roughly 3%.

Based on this information, four parameter sets will be used within this chapter to investigate the effects of this anisotropy on the model. The maximum anisotropy in t will be set to 10% of t, so that $t_x = 0.9t_y$. Cases where $t_x = 0.925t_y$, $t_x = 0.95t_y$, and $t_x = 0.975t_y$ will also be examined, with the latter being the closest to the 5° distortion described above. Parameter sets involving $t_y > t_x, J_y > J_x$ will also be examined, since the twenty-four site cluster is not rotationally invariant under $\pi/4$ rotations. The values for J based on these t values are summarised in Table 4.1. The extended $t - J$ model parameters t' and t'' have been excluded from the data in this chapter.

t_x	J_x	Bond Angle (^{o})
1.000	0.400	0.0
0.975	0.380	6.4
0.950	0.361	9.1
0.925	0.342	11.2
0.900	0.324	12.9

Table 4.1: Values for t_x to be used in this chapter with corresponding values for J_x, with $t_y = 1$ and $J_y = 0.4$. The same values will also be used for t_y and J_y, with $t_x = 1$ and $J_x = 0.4$.

While Chapter 3 focussed on results from a twenty-site cluster, this chapter will primarily focus on the twenty-four site cluster shown in figure 4.1. The stripes found

21	22	23	24
17	18	19	20
13	14	15	16
9	10	11	12
5	6	7	8
1	2	3	4

Figure 4.1: The 4x6 twenty four-site cluster that will be used in this chapter. Within this chapter, the direction running from site 1 to site 21 shall be labelled as the y-direction, while the direction running from site 1 to site 4 shall be labelled the x-direction.

in the LTT phase of $La_{1.6-x}Sr_xNd_{0.4}CuO_4$ lie directly along the copper and oxygen bonds. In order to find such stripes on small clusters, the cluster should not be tilted in a manner that would make it impossible to generate such a stripe using periodic boundary conditions. Such is the case for most small clusters, including the twenty-site, twenty six-site, and thirty two-site clusters. The 4x4 sixteen-site cluster has the required symmetry, but is plagued by finite size effects. The 4x6 twenty four-site cluster is the next available choice. All the data for this chapter has been obtained from this cluster.

4.3 Binding Energy

The analysis of the anistropic model will once again begin with the binding energy. This property is somewhat more pertinent for the LTT phase than the LTO phase, as the levels of doping in which the stripes occur are higher for the LTT phase. The doping percentage for two holes on a twenty-site cluster, for example, is $x = 0.083$, which lies within a doping regime in which the stripes are found in this compound. This justifies further the examination of two-hole states when probing for stripe behaviour in this cluster. The binding energies for the twenty four-site cluster as a function of
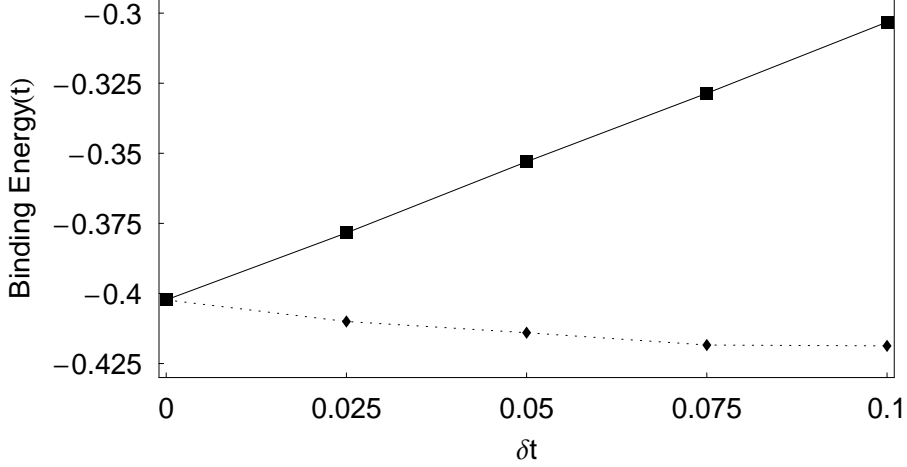
Figure 4.2: The binding energy of the twenty four-site cluster as a function of the level of anisotropy in t. The boxes correspond to $t_x < t_y$, while the diamonds correspond to $t_x > t_y$.

the anisotropy are shown in figure 4.2. A strong tendency towards binding can be seen when the anisotropy is introduced in either direction. As the level of anisotropy is increased, the results indicate a suppression of binding for the $t_x < t_y$ case, and an enhancement of binding for the $t_x > t_y$ case. The relation between δt and the BE is approximately linear in the anisotropic t_x case, where a change of $0.1t$ in t_x results in an increase of $0.0991t$ in BE. The anisotropic t_y case does not follow the same linear relation, with the change in BE diminishing as δt is increased. The total decrease in BE is only $0.0164t$ for this case over the same change in δt. The suppression of the binding energy in the $t_x < t_y$ case is insufficient to break the bound state, with BE at the highest level of anisotropy being $-0.3032t$. If the linear relation holds beyond these levels of anisotropy, then values for t_x lower than $0.6t_y$ would be required to cause the binding energy to become positive. It is then safe to assume that two holes doped into the model using this cluster form a bound state for the parameter values used.

4.4   Charge Ordering

The binding energy results from section 4.3 show the formation of bound pairs within the twenty four-site cluster. The orientation of these bound pairs within real space should also be analysed. As in Chapter 3, this shall be measured using the HHCF.

The results for the HHCF on the twenty four-site cluster are shown graphically in figure 4.3. The square indicates the location of the first hole and the size of the circle indicates the relative probability of finding the second hole at that site. The results found using isotropic parameters show some interesting behaviour. Even without the presence of anisotropic parameters, the HHCF is highly anisotropic. The largest probability of finding the second hole is at the sites horizontal to the first hole, which corresponds to the large circles in figure 4.3, with slightly smaller probabilities just above and below these sites. The three sites in the horizontal direction that contain the largest circles have a combined probability of 33.25% of finding the second hole at these three sites. If expanded to a 3 X 3 square formed with the largest circles then the probability increases to 72.89%. Hence, the two holes are essentially aligned in a horizontal row. When the periodicity of the lattice is accounted for and we extend these results to the infinite two-dimensional lattice, the result is a horizontal stripe-like structure, with pairs of holes aligning in a single row with a distance of $2a$ between holes in the row, and a distance of $6a$ between the rows. This type of alignment can be seen more clearly in figure 4.4.

When the anisotropy is introduced into the parameters, the probability of the second hole residing in the 3x3 square discussed above diminishes when $t_x < t_y$, and strengthens when $t_x > t_y$. For the anisotropic x parameters in the most extreme case, the probability of lying within the square is 68.95%, a reduction of only 3.94%. The probability becomes 74.49% when the most extreme anisotropy is used in the y-direction, an increase of 1.60%. Both changes are quite small given the high level of anisotropy. This further supports the claim that the absence of $\pi/4$ rotational
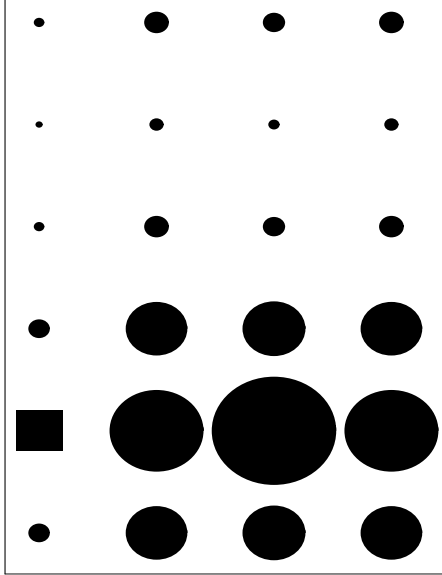
Figure 4.3: The HHCF for two holes on the twenty four-site cluster with $J = 0.4t$ and periodic boundary conditions. The black square indicates the location of the first hole, while the sizes of the circles indicate the probability of finding the second hole at that site. The largest circle corresponds to a probability of 13.25%, while the smallest to a probability of 0.77%.

symmetry in the ground state effectively quenches any effect from the anisotropic parameters, as seen in the twenty-site one-hole results from the previous chapter.

The total hole momentum of the system is $\vec{k} = (\pi, 0)$, which suggests a net motion of the holes in the x-direction. Thus the bound pairs appear to move along the direction of the stripe. The high correlations for the (2,-1) and (2,1) positions seem to suggest that the holes do have a limited amount of motion in the y-direction. The results are similar to those seen in Chapter 3, with the second hole having a high probability of placement on a site that is degenerate with itself by a rotation of $\pi/2$. However, results for the HHCF on a 12 x 12 cluster within the $t - J$ model using the Hartree-Fock technique have also shown orientation of the holes into horizontal stripes with spacing of $2a$ [76], so this may indeed be indicative of the ground state of the model.
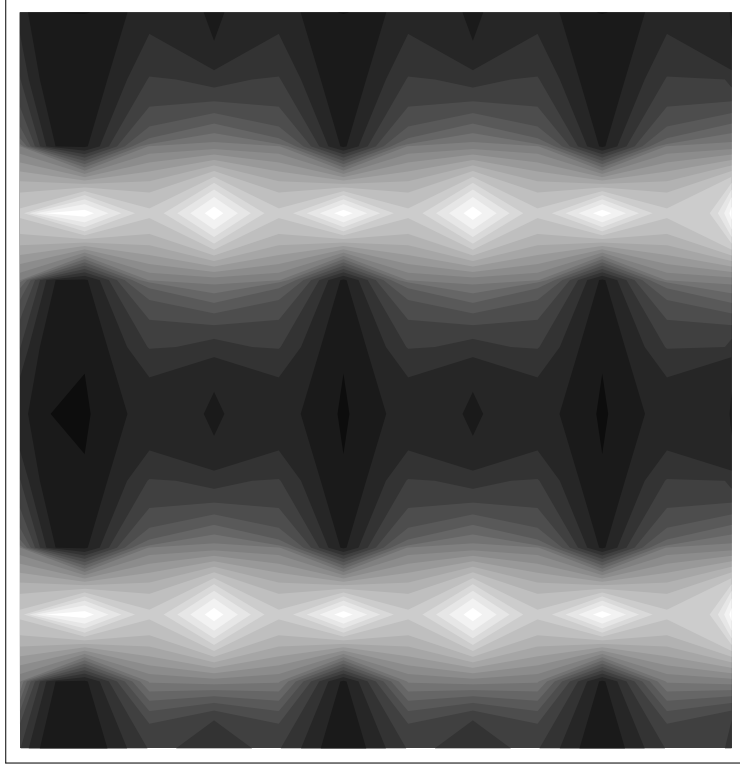
Figure 4.4: A graphical view of the hole alignment seen in the twenty four-site cluster. A total of six clusters are shown, in 2 rows of 3 columns, aligned according to the boundary conditions for this cluster. The light and dark regions denote high and low probability of hole placement, respectively.

4.5 Magnetic Properties

The magnetic properties of the model are again the most important signatures of stripes. The presence of a spin wave in the numerical results is a good indication of the presence of a stripe in the model. IC peaks in the static magnetic structure factor are also a key experimental signature of stripes.

Results for the SSCF using the isotropic parameter set are shown on the left side of figure 4.5. The results are presented with the inclusion of the staggering term outlined in section 3.3. Even without the anisotropic parameters, the results are extremely anisotropic. The correlations in the x-direction are highly AF, while in the y-direction the correlations are somewhat diminished. In fact, the AF behaviour in
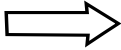
0.0111	0.0136	0.0111	0.0161		0.0182	0.0231	0.0182	0.0249
0.0379	0.0376	0.0379	0.0328		0.0472	0.0494	0.0472	0.0387
0.1062	0.2012	0.1062	0.1061		0.1066	0.2311	0.1066	0.0975
0.3084	[0.6875]	0.3084	0.1374	⟹	0.2764	[0.6875]	0.2764	0.1202
0.1062	0.2013	0.1062	0.1061		0.1066	0.2311	0.1066	0.0975
0.0379	0.0376	0.0379	0.0328		0.0472	0.0494	0.0472	0.0387

Figure 4.5: The results for the staggered SSCF for the twenty four-site cluster with two holes. On the left are the results using isotropic parameters, while on the right are the results using $t_x = 0.9t_y$. $J = 0.4t$ in both cases.

the y-direction almost vanishes at a distance of only two lattice spacings. This implies that AF behaviour is somewhat frustrated in this direction, yet remains strong in the x-direction.

The effects of the introduction of anisotropy into the model can be seen on the right side of figure 4.5. The results shown are for the case where $t_x = 0.9t_y$. This reduction of the hopping in the x-direction strengthens the AF correlations in the y-direction, while weakening them in the x-direction. The change is also linear, as seen in figure 4.6, which shows the change in nearest neighbour correlation as a function of δt. The difference in magnitude compared to the isotropic state is approximately the same in each direction, with a change of 0.0254 in the y-direction and a change of 0.0321 in the x-direction. If these numbers are expressed as a percentage of the original isotropic values, then the y-direction change is 13.2% while the x-direction change is 10.6%. With reduced hopping parameters in the y-direction, the changes are reversed. The x-direction nearest neighbour AF correlations are increased by 0.0243, while those in the y-direction are reduced by 0.0282. These changes in magnitude are
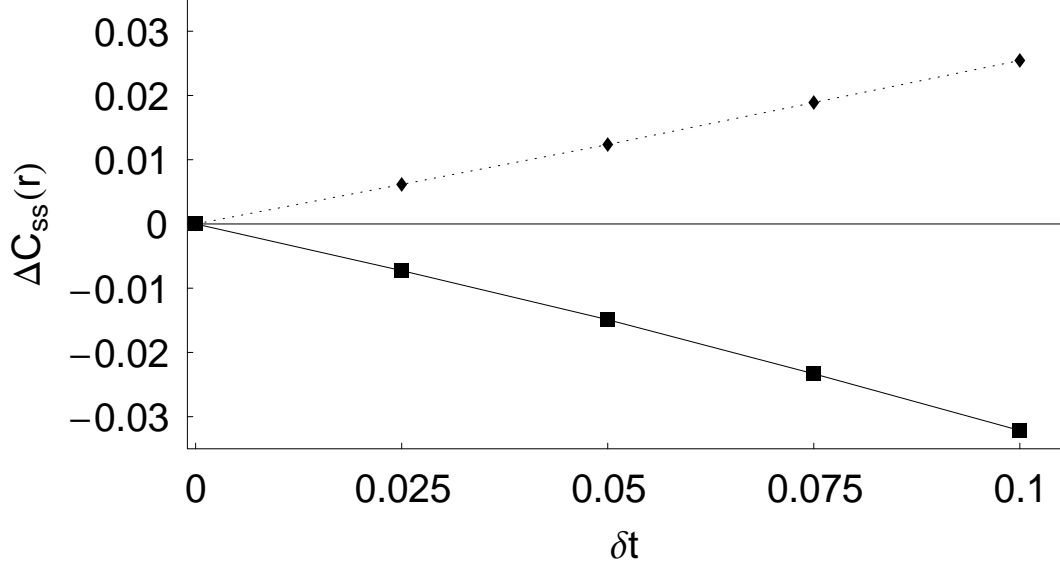
Figure 4.6: The difference in magnitude of the SSCF at nearest neighbour distance as a function of the anisotropy in t in the x-direction ($t_x < t_y$). The diamonds are for $\vec{r} = (0, a)$, while the boxes are for $\vec{r} = (a, 0)$.

similar to those seen in the $t_x = 0.9t_y$ case, while the percentage changes in this case are 8.0% and 14.6% for the x- and y-directions, respectively.

The behaviour of the function is similar to that seen in section 3.3, where the introduction of anisotropy caused a "splitting" of the correlation function results between the $x + y$ and $x - y$ directions. In the LTT case, where the anisotropy is along the x and y axes, the values are "split" between the x and y directions. However, unlike the results from Chapter 3, the values for the staggered SSCF at a given distance are not conserved with the introduction of the anisotropy. For example, the sum of the nearest neighbour SSCF values in the isotropic case is -0.5096, while in the anisotropic case the sum is -0.5075. This may be due to the already anisotropic nature of the cluster itself.

The appearance of spin modulation in a certain direction is clear in all cases shown. The isotropic results show a strong modulation of spin in the y-direction, perpendicular to the aligned pairs of holes seen in the previous section. This is indeed an indication of stripe behaviour. The introduction of reduced hopping in

the x-direction into the model reduces this modulation, which can be viewed as a weakening of the stripe. This agrees with the results presented for the HHCF. The introduction of reduced hopping in the y-direction reverses these changes, further modulating the spins in the y-direction. This indicates a strengthening of the stripe phase, which also agrees with the previous results.

In order to examine the existence of IC peaks within the model, $S(\vec{q})$ (equation 3.3) will again be used. While the twenty-site cluster used in Chapter 3 had no wave vectors along the lines $\vec{q} = (\pi, 0) \rightarrow (\pi, \pi)$ and $\vec{q} = (0, \pi) \rightarrow (\pi, \pi)$, the twenty four-site cluster has four wave vectors along the former line and three along the latter. This facilitates the investigation of IC peaks within this cluster. In addition to the two-hole state examined throughout this chapter, results from the zero- and one-hole states will be included. These results will provide further evidence into the existence of IC peaks in a similar manner to that seen in Chapter 3.

	$\vec{q}$	0 holes	1 hole
$\vec{q} = (0, \pi) \rightarrow (\pi, \pi)$	$(0, \pi)$	0.4724	0.5092
	$(\frac{\pi}{2}, \pi)$	0.8392	0.8475
	(π, π)	5.5998	4.1140
$\vec{q} = (\pi, 0) \rightarrow (\pi, \pi)$	$(\pi, 0)$	0.5325	0.5118
	$(\pi, \frac{\pi}{3})$	0.6828	0.6671
	$(\pi, \frac{2\pi}{3})$	1.3025	1.3180
	(π, π)	5.5998	4.1140

Table 4.2: Results for $S(\vec{q})$ on the twenty four-site cluster with zero and one holes. $J = 0.4t$ for both cases, with $t' = t'' = 0$.

The zero and one hole results for $S(\vec{q})$ within the twenty four-site cluster are shown in table 4.2. Shown in this table are isotropic results for the wave vectors most pertinent to the examination of IC peaks. Six wave vectors are shown, all of which lie along the lines $\vec{q} = (\pi, 0) \rightarrow (\pi, \pi)$ and $\vec{q} = (0, \pi) \rightarrow (\pi, \pi)$. The reduction in the

$\vec{q} = (\pi, \pi)$ result as the doping is increased from zero holes to one hole can clearly be seen, and this agrees with the results found in Chapter 3. However, this point marks the only significant difference between the results for each doping level. The similarity between the results for each level of doping at wave vectors other than $\vec{q} = (\pi, \pi)$ is quite plain, suggesting that there is little change in the magnetic structure upon removal of an electron from the zero hole ground state. Also of note in these results is the disparity between the two directions shown. In a square cluster with isotropic parameters, the results along each of these lines should be equivalent. This is not seen here, as can be seen from the values for $\vec{q} = (0, \pi)$ and $\vec{q} = (\pi, 0)$. However, the disparity is fairly small, particularly in the one hole case. Numerically speaking, the $\vec{q} = (\pi, 0)$ value is 12.7% larger than the $\vec{q} = (0, \pi)$ value in the zero hole case, and only 0.51% larger in the one hole case. The values for the other $\vec{q}$ values presented are more difficult to compare, since the points along each line are not rotations of each other. However, it is worth noting that the value for the $\vec{q} = (\pi/2, \pi)$ wave vector lies between the values for $\vec{q} = (\pi, \pi/3)$ and $\vec{q} = (\pi, 2\pi/3)$, suggesting a constantly increasing function for $S(\vec{q})$ as $\vec{q}$ approaches $\vec{q} = (\pi, \pi)$.

	$\vec{q}$	$t_x = t_y$	$t_x = 0.9t_y$	$t_y = 0.9t_x$
$\vec{q} = (0, \pi) \rightarrow (\pi, \pi)$	$(0, \pi)$	0.3952	0.4847	0.3224
	$(\frac{\pi}{2}, \pi)$	0.7474	0.8540	0.6684
	(π, π)	2.8255	2.8940	2.6623
$\vec{q} = (\pi, 0) \rightarrow (\pi, \pi)$	$(\pi, 0)$	0.6428	0.5573	0.7423
	$(\pi, \frac{\pi}{3})$	0.8278	0.7206	0.9390
	$(\pi, \frac{2\pi}{3})$	1.7632	1.6353	1.8558
	(π, π)	2.8255	2.8940	2.6623

Table 4.3: Results for $S(\vec{q})$ on the twenty four-site cluster with two holes. The corresponding values for J are shown in table 4.1.

The results for $S(\vec{q})$ within the twenty four-site cluster with two holes are presented

in table 4.3. The results for all parameter sets again show a peak at the $\vec{q} = (\pi, \pi)$ location, indicative of the strong AF correlations present. The isotropic results show much higher values for $S(\vec{q})$ along the $\vec{q} = (\pi, 0) \rightarrow (\pi, \pi)$ line than the $\vec{q} = (0, \pi) \rightarrow (\pi, \pi)$ line, with the $(\pi, 0)$ value being approximately 1.60 times larger than the $(0, \pi)$ value. This is a much larger difference than that seen in the zero- and one-hole cases. To better illustrate the differences between the one-hole case and the two-hole case, a graph of the these results along each of the aforementioned lines can be seen in figure 4.7. The two-hole results clearly show a suppression of $S(\vec{q})$ along the $\vec{q} = (0, \pi) \rightarrow (\pi, \pi)$ line when compared to the one-hole case, and an enhancement of $S(\vec{q})$ along the $\vec{q} = (\pi, 0) \rightarrow (\pi, \pi)$ line. This is suggestive of the formation of IC peaks along the $\vec{q} = (\pi, 0) \rightarrow (\pi, \pi)$ direction. From these results, it is doubtful that if IC peaks are indeed seen in this cluster at this level of doping that they would be equivalent along each of these lines. This would imply the existence of a unidirectional stripe phase, in agreement with the experimental results of Wakimoto *et al.* [28].

The effects of the introduction of anisotropy into the model is also shown in table 4.3. These results show a reduction of $S(\vec{q})$ values along the $\vec{q} = (\pi, 0) \rightarrow (\pi, \pi)$ line with the introduction of anisotropic x parameters, and an increase in $S(\vec{q})$ values along the $\vec{q} = (\pi, 0) \rightarrow (\pi, \pi)$ line. The opposite is true with the introduction of anisotropic x parameters. In accordance with the discussion of the stripe signature above, this would appear to indicate the enhancement of the stripe phase with the introduction of anisotropic t_y, and suppression of the stripe phase with the introduction of anisotropic t_x. This is similar behaviour to that seen from the SSCF and HHCF results for this cluster.

4.6 Correlations Across Holes

One of the major aspects of the stripe phase in $La_{1.6-x}Sr_xNd_{0.4}CuO_4$ is the AF phase boundary that results in the IC magnetic structure. Tranquada *et al.* [22] proposed
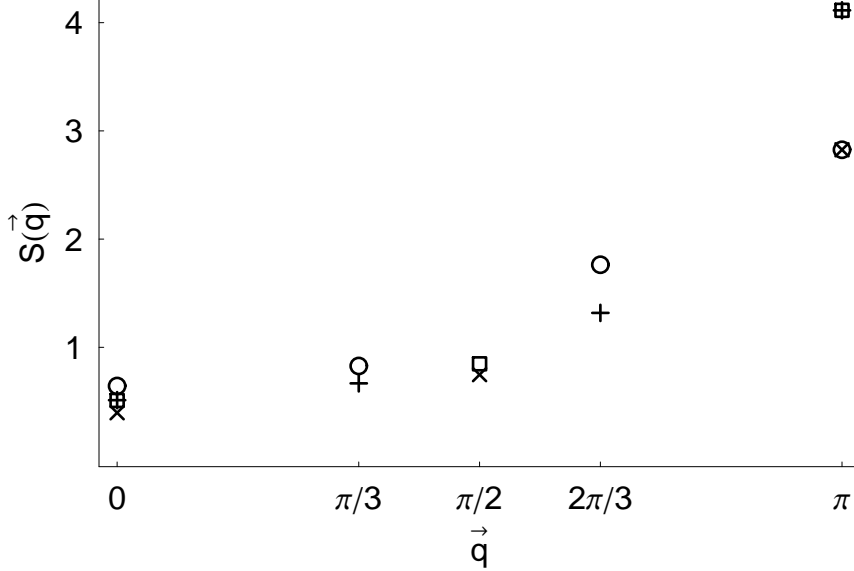
Figure 4.7: $S(\vec{q})$ as a function of $\vec{q}$ within the twenty four-site cluster. The squares and plus symbols denote results for the one-hole case along the $\vec{q} = (0, \pi) \rightarrow (\pi, \pi)$ and $\vec{q} = (\pi, 0) \rightarrow (\pi, \pi)$ directions, respectively. The crosses and circles denote results for the two-hole case along the same lines. For the results along the $\vec{q} = (0, \pi) \rightarrow (\pi, \pi)$ line, the $\vec{q}$ values labelled are for q_x, with $q_y = \pi$. For the results along the $\vec{q} = (\pi, 0) \rightarrow (\pi, \pi)$ line, the $\vec{q}$ values labelled are for q_y, with $q_x = \pi$.

that the existence of AF correlations across holes contained within the stripe would cause this type of magnetic structure. These correlations are perpendicular to the stripe. Within the $t - J$ model, these correlations can be measured using the 3-site correlation function (3SCF), defined as

$$C_{\sigma,\mu}(\vec{r}) = \frac{1}{N_h} \sum_i \langle E_0^N | n_{i-\vec{r},\sigma}(1 - n_{i,\uparrow})(1 - n_{i,\downarrow})n_{i+\vec{r},\mu}|E_0^N \rangle. \tag{4.2}$$

This function measures the correlations between an electron of spin σ at site $i - \vec{r}$ and an electron of spin μ at site $i + \vec{r}$ surrounding a hole at site i. This can be viewed as measuring the local spin background around the holes. Previous results for this function have shown the existence of strong AF correlations across holes within the $t - J$ model [77, 78]. The implication of this type of correlation is that holes have an increased chance of hopping to a nearest neighbour site if the spins on either side

64

| | | t_x/t_y | | |
		1.0/1.0	0.9/1.0	1.0/0.9
x-direction	FM	0.3261	0.3411	0.3175
	AF	0.4739	0.4733	0.4822
y-direction	FM	0.3796	0.3718	0.3845
	AF	0.5745	0.5897	0.5622

Table 4.4: Results from the 3SCF showing the AF and FM correlations between spins on either side of a hole, in each direction, for the twenty four-site cluster. Note that the values for each case do not add up to 1. The missing probability is the chance that 2 holes are placed at nearest neighbour distance in that direction.

of the hole (along the axis of the hop) are antiferromagnetically aligned. After the hole hops, the two spins will now be nearest neighbours and be antiferromagnetically aligned, which is energetically favourable. Ferromagnetic correlations across the hole would frustrate the antiferromagnetism after a hop, thus reducing the probability that the hole will hop in that direction.

The 3SCF is ideal for examining these correlations within the twenty-four site cluster, as the stripes are not tilted as they are in the twenty-site cluster. This allows us to examine the AF correlations across holes within the stripe perpendicular to the direction of the stripe. Isotropic and anisotropic results for this function within the twenty four-site cluster are shown in table 4.4. The isotropic results show a strong tendency towards AF correlations across holes in both directions, with the y-direction correlations being particularly strong. As discussed above, this would seem to indicate motion of holes predominantly in the y-direction. The ground state wave vector is $(\pi, 0)$, signifying a net zero momentum in the y-direction. This infers that the holes would be moving in opposite directions. Net motion of holes in the x-direction is also implied by the $(\pi, 0)$ momentum of the ground state, and the strong AF correlations also seen in this direction favour this behaviour.

The anisotropic results seen in the table are very similar to the isotropic results. Lowering the exchange parameters in the x-direction results in an increase in the

ferromagnetism across holes in that direction, while the AF correlation for the x-direction is essentially unchanged from the isotropic state. These results infer a slight reduction of hole motion in the x-direction, due to the magnetic frustration caused. The opposite is true of the y-direction results, with higher AF and diminished ferromagnetic correlations. When the anisotropy is introduced in the y-direction, the change is similar in magnitude, but opposite in sign. This obviously suggests a strengthening of the stripe, which agrees with the results from the two functions already examined. However, the degree of change for this function when either type of anisotropy is introduced is quite small, with the greatest percentage change from the isotropic state being roughly 4.6%.

This 3SCF data assists in clarifying the results seen for the SSCF. With the holes being predominantly displaced from one another in the x-direction, and the spins having a strong tendency to antiferromagnetically align across these holes in the y-direction, an AF frustration is introduced into the lattice in the y-direction. When the strong AF correlations in the x-direction are coupled with the results from the 3SCF and the HHCF, the local spin structure around the holes is as seen in figure 4.8. The HHCF suggests that the holes be placed two lattice spacings apart, while the 3SCF implies that the spins surrounding these holes should be antiferromagnetically aligned in both the x- and y-directions. Using these results as a starting point, the remainder of the spins are arranged as antiferromagnetically as possible. Note that in the example configuration shown, the antiferromagnetism becomes frustrated in the y-direction at the cluster boundary, which would serve to weaken the results for the SSCF in the y-direction. The x-direction correlations would remain strong, as there is no frustration present in this direction. This type of structure, along with perturbations of it, would appear to be the most dominant configurations of charge and spin within the model based on the results from the correlation functions examined within this chapter. These preferred states are weakened by the inclusion
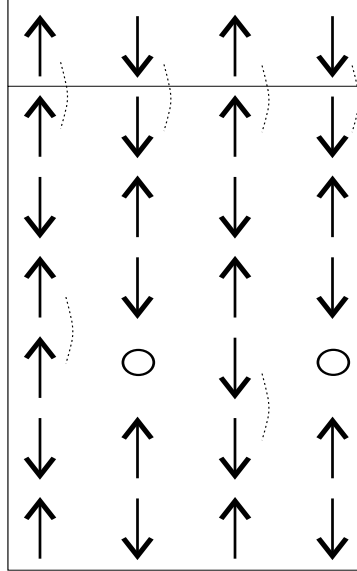
Figure 4.8: An example of a preferred configuration of spins and holes for the twenty four-site cluster with two holes. The circles denote the positions of the holes, while the up and down arrows denote spin up and spin down electrons, respectively. The bottom row of the cluster is repeated at the top of the figure to clearly show the relation between spins at the cluster boundary. This structure is periodic in the x-direction. Broken AF bonds are shown with the curved and dotted lines.

of $t_x < t_y$, and strengthened by $t_x > t_y$. Increasing the anisotropy further in the x-direction could result in an altering of this state. Note that a lower degree of magnetic frustration in the model, and therefore lower energy, could be achieved if the correlations across the holes in the y-direction were FM. However, the 3SCF results appear to indicate that antiferromagnetism in the region containing no charge is secondary to having strong AF correlation across the holes in this direction. Since this latter type of correlation is found in stripe phases, this provides further evidence that a stripe phase is indeed preferred for this cluster.

4.7   Extreme Anisotropy

As seen in the results for the twenty four-site cluster presented in the preceding sections, the introduction of anisotropic t and J parameters in the x-direction weakens
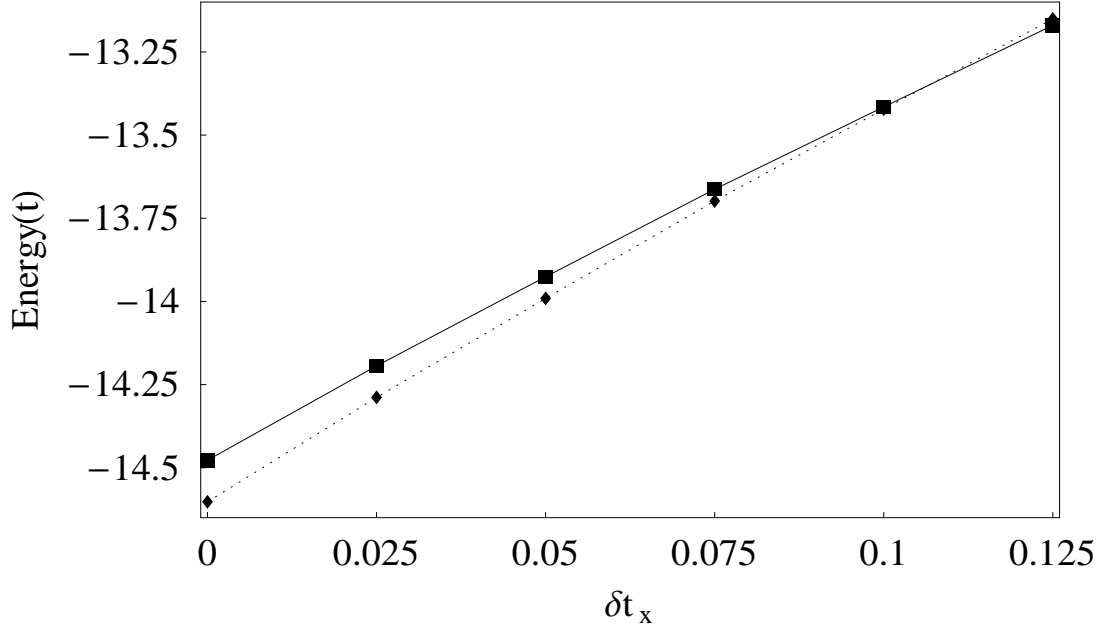
Figure 4.9: Energy of the twenty four-site cluster as a function of δt_x. The diamonds denote the $\vec{k} = (\pi, 0)$ energies, while the boxes denote the $\vec{k} = (0, 0)$ energies.

the spin correlations in the x-direction while strengthening them in the y-direction. This indicates a weakening of the state described in section 4.6, where the holes are aligned in a horizontal row with the local spin background seen in figure 4.8. It is worthwhile to investigate the possibility of disturbing this state even further by introducing an even higher level of anisotropy. The SSCF results appear to indicate that hole motion in the x-direction is being hampered as the level of anisotropy in this direction is increased, so that motion in this direction would eventually cease if the anisotropy continued to increase. To this end, results from a case involving $J_x = 0.306$ and $t_x = 0.875$ will be presented in order to show the effects of extreme anisotropy on this cluster.

The energies of the model as a function of the level of anisotropy are shown in figure 4.9, for the wave vectors $\vec{k} = (\pi, 0)$ and $\vec{k} = (0, 0)$. Up to a level of $t_x = 0.9t_y$, the ground state wave vector remains $\vec{k} = (\pi, 0)$. However, the ground state changes
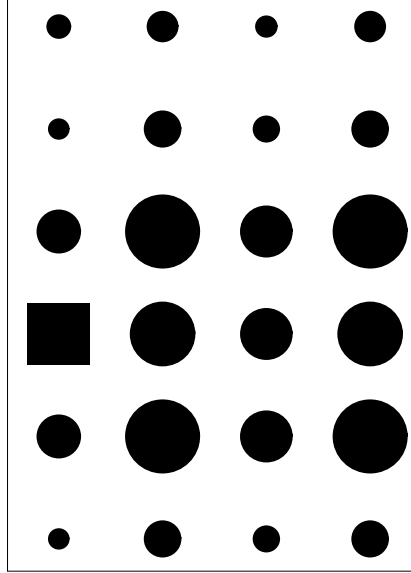
Figure 4.10: HHCF results for the twenty four-site cluster with two holes under extreme anisotropy ($t_x = 0.875t_y$). The black square indicates the location of the first hole, while the sizes of the circles indicate the probability of finding the second hole at that site. The largest circle corresponds to a probability of 7.23%, while the smallest to a probability of 2.09%.

to a $\vec{k} = (0,0)$ ground state between $t_x = 0.9t_y$ and $t_x = 0.875t_y$. This represents a change in rotational symmetry from the $\vec{k} = (\pi, 0)$ ground state, which would affect all the values for the correlation functions. Each of these functions will be examined in turn to determine these effects.

Upon examination of the charge ordering within the $\vec{k} = (0,0)$ ground state using the HHCF, the results shown in figure 4.10 are found. The probability of finding the second hole at a distance of $2a$ away in the x-direction, previously the site with highest probability, has diminished by roughly 57% from 0.1191 to 0.0507. No remnant of the stripe phase can be seen in this data. The results are now similar to those previously seen for this function in the $t - J$ model, with holes having the highest probability of being displaced by a distance of $\sqrt{2}a$ or a. The probability that the second hole is at these two sites is 0.07227 and 0.06320, respectively. The holes now appear to prefer to lie on neighbouring columns as opposed to on the 3x3 square described in
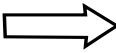
0.0182	0.0231	0.0182	0.0249	0.0550	0.0817	0.0550	0.0618
0.0472	0.0494	0.0472	0.0387	0.0693	0.0926	0.0693	0.0548
0.1066	0.2311	0.1066	0.0975	0.0973	0.2953	0.0973	0.0767
0.2764	0.6875	0.2764	0.1202	0.1985	0.6875	0.1985	0.0802
0.1066	0.2311	0.1066	0.0975	0.0973	0.2953	0.0973	0.0767
0.0472	0.0494	0.0472	0.0387	0.0693	0.0926	0.0693	0.0548

Figure 4.11: Staggered SSCF results for the twenty four-site cluster with two holes under extreme anisotropy ($t_x = 0.875t_y$). The values on the left are for $t_x = 0.9t_y$, provided for comparison. The boxed results denote the location of the first spin ($r = 0$).

section 4.4. Also of note is the increased probability of holes being displaced from one another in the y-direction when the extreme anisotropy is introduced. These probabilities are approximately double the values for the $t_x = 0.9t_y$ case. However, the probability of a nearest neighbour alignment of spins in the y-direction is only 0.0429, considerably smaller than the 0.0632 probability of a nearest neighbour pair in the x-direction. Therefore the state where the holes are vertically aligned could correspond to a first order perturbation of the preferred state where the holes are in neighbouring columns.

The effect of the extreme anisotropy on the static magnetic properties of the model can be seen in the SSCF results shown on the right side of figure 4.11. The results for the case where $t_x = 0.9t_y$ are shown on the left for comparison. The change is quite substantial, with the stronger AF correlations now being found in the y-direction as opposed to the x-direction. The magnitude of the increase for all values directly along the y-axis ranges from 0.0432 to 0.0642, while the decrease in the values along

the x-axis is roughly the same magnitude. This implies that the spin modulation has rotated by 90°, and that the stripe signature seen in the results with lower levels of anisotropy has been destroyed. This agrees with the results seen for the HHCF. The y-direction correlations remain fairly strong even at a distance of $3a$ away, suggesting strong long-range AF behaviour along this direction. The frustration in the magnetic correlations in the x-direction may be due to the increased probability of nearest neighbour placement of holes in this direction.

The change in the static magnetic properties can also be observed with $S(\vec{q})$. The results for this quantity shown in table 4.5 illustrate a drastic change from the $t_x = 0.9t_y$ case to the $t_x = 0.875t_y$ case. All values along the $q = (0, \pi) \rightarrow (\pi, \pi)$ line experience a large enhancement for both the one- and two-hole cases, while the opposite is true of the $q = (\pi, 0) \rightarrow (\pi, \pi)$ line. The changes are similar to those seen when comparing the isotropic case to the $t_x = 0.9t_y$ case, but the magnitude of the change from the latter case to the $t_x = 0.875t_y$ case is much more pronounced. For example, the change in magnitude for the $S(\vec{q})$ results from the isotropic case to the $t_x = 0.9t_y$ case was roughly equal to 0.1, for all wave vectors except $q = (\pi, \pi)$. The magnitude of the change for these same wave vectors has now grown to 0.2-0.4 when δt is increased from $\delta t = 0.10$ to $\delta t = 0.125$, a very drastic increase.

The results for $S(\vec{q})$ now appear to exhibit a state with stronger results along the $q = (0, \pi) \rightarrow (\pi, \pi)$ line than the $q = (\pi, 0) \rightarrow (\pi, \pi)$ line, in contrast to the results seen for this function when isotropic parameters are used. This conclusion is again difficult to assert since the wave vectors along each line are not equivalent, with the exception of the endpoints. The final column in table 4.5 shows the one-hole results at this level of anisotropy. These values are provided to show the similarity between the one-hole and two-hole $S(\vec{q})$ results at all $q \neq (\pi, \pi)$. Note that this level of similarity is not seen in the isotropic results, where it was strongly suggested that the two-hole results were indicative of IC peaks. The results for the $t_x = 0.875t_y$ case would then

| | $\vec{q}$ | 2 holes | | 1 hole |
		$t_x = 0.9t_y$	$t_x = 0.875t_y$	$t_x = 0.875t_y$
$\vec{q} = (0,\pi) \rightarrow (\pi,\pi)$	$(0,\pi)$	0.4847	0.7766	0.7419
	$(\frac{\pi}{2},\pi)$	0.8540	1.1396	1.0223
	(π,π)	2.8940	3.1232	4.4405
$\vec{q} = (\pi,0) \rightarrow (\pi,\pi)$	$(\pi,0)$	0.5573	0.3500	0.3846
	$(\pi,\frac{\pi}{3})$	0.7206	0.5657	0.5269
	$(\pi,\frac{2\pi}{3})$	1.6353	1.1920	1.1078
	(π,π)	2.8940	3.1232	4.4405

Table 4.5: Results for $S(\vec{q})$ on the twenty four-site cluster with one and two holes, for $t_x = 0.875t_y$.

appear to indicate that the incommensurability has been removed with this level of anisotropy.

The 3SCF also appears affected in a similar manner by the extreme anisotropy. Results for this function are shown in table 4.6. The most prominent result is the reduction of the AF correlations and enhancement of the FM correlations in the x-direction. The change in the FM correlations in this direction is quite pronounced, with a 26.5% increase in this value when compared to the $t_x = 0.9t_y$ case. The equality of the AF and FM correlations in the extreme anisotropy case would suggest that hole motion in the x-direction is no longer preferred. The changes in the y-direction correlations are similar in sign to that of the x-direction, but dissimilar in magnitude. The AF correlations are most affected, with the value for the 3SCF being reduced by 10.6%. The FM correlations remain roughly the same. Even with these changes, the y-direction AF correlations remain much stronger than the FM correlations with this level of anisotropy, which would suggest that hole motion in the y-direction is only slightly diminished.

		t_x/t_y	
		0.9/1.0	0.875/1.0
x-direction	FM	0.3411	0.4316
	AF	0.4733	0.4420
y-direction	FM	0.3718	0.3869
	AF	0.5897	0.5273

Table 4.6: Results from the 3SCF showing the AF and FM correlations between spins on either side of a hole, in each direction, for the twenty four-site cluster in the presence of extreme anisotropy ($t_x = 0.875t_y$). The results for $t_x = 0.9t_y$ are also included for comparison.

4.8   Summary

The results presented in this chapter focus on the LTT phase of cuprate materials, specifically $La_{1.6-x}Sr_xNd_{0.4}CuO_4$. This phase has anisotropy between the a- and b-directions on-plane, which can easily be incorporated into numerical models using anisotropic parameters. This chapter examined some of the results gained using these parameters within the $t - J$ model on a twenty four-site cluster that allows a vertical or horizontal stripe.

The HHCF results coupled with the binding energy results strongly suggest the existence of a phase involving aligned bound pairs of holes, which when viewed as a sequence of aligned clusters results in what appears to be a stripe phase. The AF correlations across the holes in the y-direction support this claim, as do the IC magnetic peaks. The SSCF results for this cluster in the x-direction also indicate the presence of an AF region of spin between the charge stripes. The spin correlations in the y-direction are diminished, possibly due to a frustration caused by the AF correlations across the holes in this direction. The anisotropic parameters served to weaken this state when the hopping was reduced in the x-direction, and strengthen it when the hopping was reduced in the y-direction. Upon introduction of an ever higher level of anisotropy in the x-direction, the stripe structure vanishes and is replaced by a state similar to that seen in other clusters within the $t - J$ model. This state

consists of holes found primarily at nearest neighbour and next-nearest neighbour distances. The results for the correlation functions in the extreme anisotropy case are still highly anisotropic, with a reduced chance of charge aligning in the y-direction, and enhanced AF spin correlations in this same direction. This is most likely due to the rectangular nature of the cluster.

Chapter 5

Conclusion

The anisotropy present on the copper oxide planes of cuprate compounds has been well illustrated in experimental data of the structure of these compounds. In most cases, the degree of anisotropy is quite small, but the impact of this small change on results gained from the model has had little study to date. The results in Chapters 3 and 4 of this work show that even small changes in the values of the parameters can clearly alter the ground state of the system. In most cases, the changes seen in the correlation functions are linear with the change in anisotropy, which represents a simple change in the ground state purely based on the values of the parameters. In other cases, such as the extreme anisotropy case studied in Chapter 4, the anisotropy produces a change in symmetry of the ground state, drastically altering its behaviour.

The difficulty of examining the LTO phase using the ED technique has been illustrated throughout Chapter 3. The appropriate doping range for the LTO phase corresponds to a single hole for the twenty-site cluster. The single hole ground state wave vector should lie at $(\pi/2, \pi/2)$, a wave vector that is not allowed in this cluster. Rather, the ground state wave vector lies near this point, and does not confer any type of symmetry to the ground state. The introduction of the anisotropic parameters is not enough to overcome the effects of the symmetry and thus the anisotropy does not seem to have any effect on the model. The two-hole cases, however, show promising results. The symmetry and ground state wave vector correspond to what should be found on the copper oxide planes. Introduction of anisotropic parameters into the two-hole systems results in a much higher degree of change than the one-hole cases,

and a strongly linear relationship can be seen between the two. While the doping concentrations are inappropriate for the LTO phase, it is quite possible that the same results could be seen in larger clusters where the doping concentration would be more appropriate. This would require either the use of a technique other than ED, or an improvement in currently available computer hardware. The examination of a two-hole state in the appropriate doping regime would require a lattice of approximately forty sites or more, which is currently beyond the largest cluster size that has been studied by ED.

The linear relationship between the change in correlation function and the level of anisotropy is worthy of future analysis. This relationship was found in both Chapters 3 and 4. For most of the cases studied using anisotropic values for either the t or t' parameters, the values for the correlation functions could be predicted based on a small number of values. The only deviation from this behaviour would be due to a change in the ground state wave vector, which would necessitate a full study of the ground state energies of the model. There also exists the possibility that this type of relationship could be proved theoretically, which would offer a predictive model for the effects of anisotropy within the $t - J$ model.

The results for $S(\vec{q}, \omega)$ in Chapter 3 show the relatively small effect of the anisotropy on this quantity. A splitting of the weight between wave vectors which are $\pi/2$ rotations was clearly seen, but this is essentially the same result gained from the $S(\vec{q})$ results. The shifting of the peak to higher or lower energy represents the most important result from this quantity. However, the shift was relatively small, and is difficult to see without plotting the difference between the isotropic and anisotropic results. This data seems to indicate that the spin gap is relatively unchanged by the anisotropic parameters. This would imply that the energy of the excited spin states is altered in a very similar manner to that of the $S = 0$ state. This possibility is easily tested, and could be the focus of future work. The effect of the anisotropic parameters

on other dynamical properties, such as the spectral function, could also be examined. This function should show a greater change due to the anisotropy than that seen in $S(\vec{q}, \omega)$, since the effects of anisotropy on states of different doping concentration was shown in Chapter 3 to be quite dissimilar.

It should be restated that one of the main reasons for examining the effects of anisotropy on the model was due to the work done by Tranquada *et al.* [22] on $La_{1.6-x}Sr_xNd_{0.4}CuO_4$, which has been shown to exhibit the LTT phase. This LTT phase could be linked to the existence of the stripe phase seen within this compound. Therefore the study of the LTT phase within the confines of the $t - J$ model and the study of the existence of stripe phases within the same model are closely tied. Within this work, the existence of a stripe phase within the model is strongly suggested, but this is certainly difficult to prove. The cluster sizes are simply too small to make any clear conclusion in regards to this issue. In addition, the boundary conditions make any kind of hole alignment have only a few available possibilities. For example, the stripe state seen in the twenty-site cluster is the only possible arrangement of holes that leads to a aligned stripe. However, the holes do prefer this alignment to any other upon instantiation of anisotropic parameters, a result which strongly suggests a striped ground state in the presence of anisotropy. The results from the twenty four-site cluster are similar, with the holes aligning themselves parallel to one axis of the cluster. Supporting evidence from other measurable quantities all agree with the notion of a stripe phase within the twenty four-site cluster in its isotropic form. While this may seem like a finite size effect at first glance, it was shown in Chapter 4 that upon instantiation of extreme anisotropy, the results from the twenty four-site cluster mimicked previous results for charge distribution, with high probabilities of holes being displaced by a or $\sqrt{2}a$. Indeed, all signatures of stripes disappear from the results for all quantities measured once the extreme anisotropy limit is reached, implying that the results seen in the isotropic state are a function of the parameters

as well as the shape of the cluster. However, it is difficult to say without doubt that this is indeed a striped phase, since the number of holes within the cluster is simply too small. The best conclusion that can be made is that the results suggest a ground state that consists of aligned pairs of holes that share the characteristics of striped phases. Further work on larger clusters with a higher overall number of holes must be analysed before the results can be conclusively named a stripe phase. It should be noted that 45° oriented diagonal stripes, such as those seen in underdoped $La_{2-x}Sr_xCuO_4$, can only be seen in very few square clusters, such as the sixteen- and thirty two-site clusters. This type of charge ordering is then quite difficult to see within the confines of small lattices.

The shape of the twenty four-site cluster used in Chapter 4 is similar to four-leg ladders used in a number of numerical works [52, 79]. The alignment of holes in these ladders appears to be the same in most studies, with bound pairs separated by two lattice spacings appearing on the rungs of the ladders. The results found here support these results, which may be indicative of a finite size effect of clusters with this shape. Examination of the same cluster with three holes should ideally result in an alignment of holes along the y-axis direction as opposed to the x-axis. This would indeed be representative of a stripe, if the same AF correlations were present across the holes. These results are not available at this time, however, and present a case for further study. The case involving extreme anisotropy presented in this chapter does remove the effect seen, but again this level of anisotropy is not physically relevant.

The intended result of Chapter 4 was to begin with an isotropic, non-striped state in the isotropic parameter case and induce a stripe phase with the introduction of the anisotropic parameters. The appearance of stripes within the twenty four-site cluster for the isotropic parameter case, and the subsequent breaking of the stripe phase when the anisotropy is increased to a high level, is certainly one of the more surprising results of this work. However, even though the results appear opposite to

what was intended, it was shown that the anisotropy can indeed have an effect on the ground state symmetry of the model. Given that the goal of this study was to examine the effects of anisotropy on the $t - J$ model, the changing of this symmetry still represents a satisfying result. The ability of the anisotropy to change the ground state of other square or rectangular clusters poses a case for further work.

In summary, the anisotropic parameters used in this study provide results that are suggestive, but not conclusive, of striped behaviour in the anisotropic $t - J$ model. The correlation functions examined are not only functions of the parameters, but of the shape of the cluster. Thus the results gained could be due to either of these two factors. The shape of the cluster also limits the study of reciprocal space, where the wave vectors are discrete for a finite lattice, yet continuous within the compounds themselves. Comparison of the two is therefore again merely suggestive rather than conclusive. In order for the results to become more applicable to real compounds, larger clusters must be analysed. Currently this can be accomplished using techniques other than ED, but these methods have their own limitations. ED continues to be a precise method that will only improve with the availability of faster computer systems, which will allow the study of the effects of anisotropy on larger clusters which can also allow stripes. One such cluster is the thirty two-site cluster, which as stated previously can support either a 45° or 90° stripe. This cluster also contains the $(\pi/2, \pi/2)$ reciprocal lattice vector, making it an ideal candidate for study of a single hole. While single hole results have been done to this date, two hole results are limited, and it this level of doping that is more pertinent to stripes. Therefore study of this particular cluster using the techniques of this work appears to be the next logical step in the analysis of the effects of anisotropy on the physics of copper oxide planes.

Bibliography

[1] H. Onnes, Comm. Leiden. 124c (November 25 1911).

[2] W. Meissner and R. Oschenfeld, Naturwiss. **27**, 787 (1933).

[3] B. Josephson, Phys. Rev. Lett. **1**, 251 (1962).

[4] J. Bednorz and K. Muller, Z. Phys. B **64**, 189 (1986).

[5] J. Gaveler, Appl. Phys. Lett **23**, 480 (1973).

[6] M. Cyrot and D. Mayou, Phys. Rev. B **41**, 4033 (1990).

[7] M. Wu *et al.*, Phys. Rev. Lett. **58**, 908 (1987).

[8] L. Landau, Soviet Physics JETP **3**, 920 (1957).

[9] N. Ashcroft and D. Mermin, *Solid State Physics* (Brooks Cole, St. Paul, 1976).

[10] M. Takigawa *et al.*, Phys. Rev. B **43**, 247 (1991).

[11] T. Imai, C. P. Slichter, K. Yoshimura, and K. Kosuge, Phys. Rev. Lett. **70**, 1002 (1993).

[12] N. Mott, Proc. P. Soc. London, Ser. A **62**, 416 (1949).

[13] C. Almason and M. B. Maple, *Chemistry of High-Temperature Superconductors* (World Scientific, Singapore, 1991).

[14] Y. Nakamura and S. Uchida, Phys. Rev. B **47**, 8369 (1993).

[15] K. Takenaka *et al.*, Phys. Rev. B **50**, 6534 (1994).

[16] J. M. Tranquada, S. M. Heald, A. Moodenbaugh, and M. Suenaga, Phys. Rev. B **35**, 7187 (1987).

[17] M. Imada, A. Fujimori, and Y. Tokura, Rev. Mod. Physics **70**, 1039 (1998).

[18] G. Shirane *et al.*, Phys. Rev. Lett. **59**, 1613 (1987).

[19] J. M. Tranquada *et al.*, Phys. Rev. Lett. **60**, 156 (1988).

[20] D. Vaknin *et al.*, Phys. Rev. Lett. **58**, 2802 (1987).

[21] N. P. Ong *et al.*, Phys. Rev. B **35**, 8807 (1987).

[22] J. Tranquada *et al.*, Nature **375**, 561 (1995).

[23] E. Dagotto, Rev. Mod Physics **66**, 763 (1994).

[24] K. Yamada *et al.*, Phys. Rev. B **57**, 6165 (1998).

[25] P. Dai, H. A. Mook, and F. Dogan, Phys. Rev. Lett. **80**, 1738 (1998).

[26] P. Dai, H. A. Mook, R. Hunt, and F. Dogan, Phys. Rev. B **63**, 054525 (2001).

[27] S. Wakimoto *et al.*, Phys. Rev. B **60**, R769 (1999).

[28] S. Wakimoto *et al.*, Phys. Rev. B **61**, 3699 (2000).

[29] S.-W. Han, E. Stern, D. Haskel, and A. Moodenbaugh, Phys. Rev. B **66**, 094101 (2002).

[30] A. R. Moodenbaugh *et al.*, Phys. Rev. B **58**, 9549 (1998).

[31] J. Tranquada *et al.*, Phys. Rev. Lett. **78**, 338 (1997).

[32] M. v. Zimmermann *et al.*, Phys. Rev. B **68**, 104515 (2003).

[33] J. Hubbard, Proc. R. Soc. London, Ser. A **276**, 238 (1963).

[34] V. Emery, Phys. Rev. Lett. **58**, 2794 (1987).

[35] P. Anderson, Science **235**, 1196 (1987).

[36] F. Zhang and T. Rice, Phys. Rev. B **37**, 3759 (1988).

[37] J. Jefferson, H. Eskes, and L. Feiner, Phys. Rev. B **45**, 7959 (1992).

[38] M. Hybertson, E. Stechel, W. Foulkes, and M. Schluter, Phys. Rev. B **45**, 10032 (1992).

[39] V. Belinicher and A. Chernyshev, Phys. Rev. B **49**, 9746 (1994).

[40] A. N. Yaresko, A. Y. Perlov, R. Hayn, and H. Rosner, Phys. Rev. B **65**, 115111 (2002).

[41] R. Singh, P. Fleury, K. Lyons, and P. Sulewski, Phys. Rev. Lett. **62**, 2736 (1989).

[42] M. Makivic and H. Ding, Phys. Rev. B **43**, 3562 (1991).

[43] A. Oosten, R. Broer, and W. Nieuwport, Chem. Phys. Lett. **257**, 207 (1996).

[44] M. Korshunov *et al.*, Journal of Experimental and Theoretical Physics **99**, 559 (2004).

[45] Z. Liu and E. Manousakis, Phys. Rev. B **45**, 2425 (1992).

[46] B. O. Wells *et al.*, Phys. Rev. Lett. **74**, 964 (1995).

[47] S.-W. Cheong *et al.*, Phys. Rev. Lett. **67**, 1791 (1991).

[48] A. Moreo and E. Dagotto, Phys. Rev. B **42**, 6283 (1990).

[49] N. Furukawa and M. Imada, J. Phys. Soc. Japan **61**, 3331 (1992).

[50] D. Poilblanc, Phys. Rev. B **49**, 1477 (1994).

[51] A. Chernyshev, P. Leung, and R. Gooding, Phys. Rev. B **58**, 13594 (1998).

[52] S. R. White and D. J. Scalapino, Phys. Rev. B **55**, R14701 (1997).

[53] A. Nazarenko *et al.*, Phys. Rev. B **51**, 8676 (1995).

[54] A. Kampf, D. Scalapino, and S. White, Phys. Rev. B **64**, 052509 (2001).

[55] S. R. White and D. J. Scalapino, Phys. Rev. B **60**, R753 (1999).

[56] T. Tohyama *et al.*, Phys. Rev. B **59**, R11649 (1999).

[57] T. Tohyama and S. Maekawa, Phys. Rev. B **49**, 3596 (1994).

[58] R. Gooding, K. Vos, and P. Leung, Phys. Rev. B **50**, 12866 (1994).

[59] T. Xiang, Phys. Rev. B **54**, R12653 (1996).

[60] P. W. Leung, B. O. Wells, and R. J. Gooding, Phys. Rev. B **56**, 6320 (1997).

[61] P. W. Leung, B. O. Wells, and R. J. Gooding, Physica C **282**, 1793 (1997).

[62] C. Kim *et al.*, Phys. Rev. Lett. **80**, 4245 (1998).

[63] L. Feiner, J. Jefferson, and R. Raimondi, Phys. Rev. B **53**, 8751 (1996).

[64] F. Becca, L. Capriotti, and S. Sorella, Phys. Rev. Lett. **87**, 167005 (2001).

[65] J. Tipper and K. Vos, Phys. Rev. B **67**, 144511 (2003).

[66] C. Lanczos, J. Res. Nat. Bur. Stand. **45**, 255 (1950).

[67] E. Dagotto and A. Moreo, Phys. Rev. D **21**, 865 (1985).

[68] J. Jaklic and P. Prelovsek, Phys. Rev. B **49**, 5065 (1994).

[69] F. Bloch, Z. Phys. **52**, 555 (1928).

[70] P. Leung, Phys. Rev. B **65**, 205101 (2002).

[71] E. Dagotto, Intl. J. Phys. B **5**, 907 (1991).

[72] M. Fujita *et al.*, Phys. Rev. B **65**, 064505 (2002).

[73] P. Horsch and W. Stephan, Physica C **185**, 1585 (1991).

[74] E. Dagotto *et al.*, Phys. Rev. B **45**, 10741 (1992).

[75] J. Jaklic and P. Prelovsek, Phys. Rev. Lett. **74**, 3411 (1995).

[76] B. Normand and A. Kampf, Phys. Rev. B **64**, 024521 (2001).

[77] G. Martins, R. Eder, and E. Dagotto, Phys. Rev. B **60**, R3716 (1999).

[78] G. Martins *et al.*, Phys. Rev. B **63**, 014414 (2001).

[79] S. R. White and D. J. Scalapino, Phys. Rev. B **57**, 3031 (1998).

[80] R. Shankar, *Principles of Quantum Mechanics* (Plenum Publishers, New York, 1994).

Appendix A

Reduction of the Hubbard model

As discussed in Chapter 2, the Hubbard model can be reduced to the $t - J$ model by making the assumption that $U \gg t$, thereby eliminating doubly occupied sites. This process is non-trivial and will be explained within this appendix. The Hamiltonian corresponding to the Hubbard model is shown in equation 2.2. Note that the U term in this model simply equals U if the site i is doubly occupied, and 0 if it is not. If one examines the copper oxide planes within the context of the Hubbard model, there exists two bands for the copper sites due to the Coulomb repulsion between two electrons on the same site. The lower Hubbard band represents the quantum states with a maximum of one electron per site, while the upper Hubbard band represents states with at least one site occupied by two electrons.

We shall define two projection operators P and Q, which will correspond to the lower and upper band, respectively. These operators will be defined by the relations $P|\psi\rangle = 0|\psi\rangle$, $Q|\psi\rangle = |\psi\rangle$ if the state $|\psi\rangle$ contains any doubly occupied sites, and $P|\psi\rangle = |\psi\rangle$, $Q|\psi\rangle = 0|\psi\rangle$ if the state $|\psi\rangle$ contains no doubly occupied sites. This also leads to the relations $QP|\psi\rangle = 0$, $PQ|\psi\rangle = 0$, $QQ|\psi\rangle = Q|\psi\rangle$, $PP|\psi\rangle = P|\psi\rangle$.

The Hubbard Hamiltonian can then be rewritten using these projection operators as

$$
\begin{aligned}
H &= -\sum_{i,j,\sigma} t_{ij}(P c_{i,\sigma}^\dagger c_{j,\sigma} P + P c_{i,\sigma}^\dagger c_{j,\sigma} Q + Q c_{i,\sigma}^\dagger c_{j,\sigma} P + Q c_{i,\sigma}^\dagger c_{j,\sigma} Q) + U \sum_i Q n_{i,\uparrow} n_{i,\downarrow} Q \\
&= H_t + H_U.
\end{aligned}
\tag{A.1}
$$

This equation explicitly accounts for the hopping of an electron from a site containing one or two electrons to a site that, after the hop, now contains either one or two electrons. Only one term is required for the U term, since the state $|\psi\rangle$ must contain doubly occupied states for this term to be non-zero.

The goal of the reduction of the Hubbard model will be to eliminate any interaction between the bands, thus allowing the study of either band individually. To this end, we must perform a canonical transformation of the Hamiltonian given above to a new

Hamiltonian $\tilde{H}$. This transformation will be done by evaluating the relation

$$\tilde{H} = e^{-i\tilde{S}^\dagger} H e^{i\tilde{S}}, \tag{A.2}$$

where $e^{i\tilde{S}}$ is a unitary operator [80]. This implies that $\tilde{S}$ is Hermitian so that $\tilde{S} = \tilde{S}^\dagger$. The operator $\tilde{S}$ is chosen in order to eliminate the interactions between the lower and upper Hubbard bands. We shall let $\tilde{S} = -iS$, where S will be chosen to be of the form

$$S = \frac{1}{U} \sum_{i,j,\sigma} [\alpha_{i,j} Q c^\dagger_{i,\sigma} c_{j,\sigma} P + \beta_{i,j} P c^\dagger_{i,\sigma} c_{j,\sigma} Q], \tag{A.3}$$

where the α and β terms are complex constants to be evaluated later. We can also write $\tilde{S}^\dagger = iS^\dagger$, where

$$S^\dagger = \frac{1}{U} \sum_{i,j,\sigma} [\alpha^\star_{i,j} P c^\dagger_{i,\sigma} c_{j,\sigma} Q + \beta^\star_{i,j} Q c^\dagger_{i,\sigma} c_{j,\sigma} P]. \tag{A.4}$$

Since $\tilde{S}$ is Hermitian, this implies that $\alpha^\star_{i,j} = -\beta_{i,j}$. The terms $\alpha_{i,j}$ and $\beta_{i,j}$ are then real, and we can write S as

$$S = \frac{1}{U} \sum_{i,j,\sigma} [\alpha_{i,j} Q c^\dagger_{i,\sigma} c_{j,\sigma} P - \alpha_{i,j} P c^\dagger_{i,\sigma} c_{j,\sigma} Q]. \tag{A.5}$$

Substitution of $\tilde{S} = -iS$, $\tilde{S}^\dagger = iS$ into equation A.2 gives

$$\tilde{H} = e^{-i\tilde{S}^\dagger} H e^{i\tilde{S}} = e^{-S} H e^{S}. \tag{A.6}$$

If one expresses the exponential functions in equation A.6 as a series, then this equation becomes

$$
\begin{aligned}
\tilde{H} &= \left(1 - S + \frac{S^2}{2!} - \ldots\right)(H_t + H_U)\left(1 + S + \frac{S^2}{2!} + \ldots\right) \\
&= H - S(H_t + H_U) + (H_t + H_U)S - SH_U S + \frac{1}{2}SSH_U + \\
&\quad \frac{1}{2}H_U SS + \ldots \tag{A.7} \\
&= H + H_1 + H_2 + \ldots, \tag{A.8}
\end{aligned}
$$

where $H_1 = H_U S - SH_U$ and $H_2 = H_t S - SH_t - SH_U S + \frac{1}{2}SSH_U + \frac{1}{2}H_U SS$. Substitution of S into H_1 gives

$$H_1 = [U \sum_k Q n_{k,\uparrow} n_{k,\downarrow} Q][\frac{1}{U} \sum_{i,j,\sigma} (\alpha_{i,j} Q c^\dagger_{i,\sigma} c_{j,\sigma} P - \alpha_{i,j} P c^\dagger_{i,\sigma} c_{j,\sigma} Q)] - SH_U \tag{A.9}$$

85

The second term is zero due to the presence of a QP operator. The first term can be written as

$$H_U S = \sum_{i,j,\sigma} \sum_k \alpha_{i,j} Q n_{k,\uparrow} n_{k,\downarrow} Q c^\dagger_{i,\sigma} c_{j,\sigma} P. \tag{A.10}$$

Since the operator P will project out all states with a doubly occupied site, and Q will project out all states that do not have a doubly occupied site, this term will only be non-zero if there is a single doubly occupied site at site i. The sum over the number operators will then equal 1. Therefore we can remove the sum over k and write this term as

$$H_U S = \sum_{i,j,\sigma} \alpha_{i,j} Q c^\dagger_{i,\sigma} c_{j,\sigma} P. \tag{A.11}$$

The SH_U term can similarly be shown to be

$$SH_U = -\sum_{i,j,\sigma} \alpha_{i,j} P c^\dagger_{i,\sigma} c_{j,\sigma} Q. \tag{A.12}$$

If these terms are now substituted into equation A.8, $\tilde{H}$ becomes

$$
\begin{aligned}
\tilde{H} &= H + H_1 + H_2 + \dots \\
&= -\sum_{i,j,\sigma} t_{i,j} (P c^\dagger_{i,\sigma} c_{j,\sigma} P + P c^\dagger_{i,\sigma} c_{j,\sigma} Q + Q c^\dagger_{i,\sigma} c_{j,\sigma} P + Q c^\dagger_{i,\sigma} c_{j,\sigma} Q) + U \sum_i Q n_{i,\uparrow} n_{i,\downarrow} Q \\
&\quad + \sum_{i,j,\sigma} \alpha_{i,j} Q c^\dagger_{i,\sigma} c_{j,\sigma} P + \sum_{i,j,\sigma} \alpha_{i,j} P c^\dagger_{i,\sigma} c_{j,\sigma} Q + H_2 + \dots
\end{aligned}
\tag{A.13}
$$

Note that if $\alpha_{i,j} = t_{i,j}$, H_1 will cancel with the two inner terms from H_t. By making this substitution, S and H become

$$
\begin{aligned}
S &= \frac{1}{U} \sum_{i,j,\sigma} t_{i,j} (Q c^\dagger_{i,\sigma} c_{j,\sigma} P - P c^\dagger_{i,\sigma} c_{j,\sigma} Q) \\
\end{aligned}
\tag{A.14}
$$

$$
\tilde{H} = -\sum_{i,j,\sigma} t_{i,j} (P c^\dagger_{i\sigma} c_{j\sigma} P + Q c^\dagger_{i\sigma} c_{j\sigma} Q) + U \sum_i Q n_{i,\uparrow} n_{i,\downarrow} Q + H_2 + \dots
\tag{A.15}
$$

This Hamiltonian has no coupling terms between bands, to order t. This is the main purpose of this reduction to the $t - J$ model. The H_2 terms still remain, however, and must be evaluated to provide the proper correction terms to the model. Substitution of S into the $H_t S$ and $S H_t$ terms of H_2 gives

$$
\begin{aligned}
H_t S &= -\sum_{i,j,\sigma} t_{i,j} (P c^\dagger_{i\sigma} c_{j\sigma} P + P c^\dagger_{i\sigma} c_{j\sigma} Q + Q c^\dagger_{i\sigma} c_{j\sigma} P + Q c^\dagger_{i\sigma} c_{j\sigma} Q) \times \\
&\quad \sum_{m,n,\mu} \frac{t_{m,n}}{U} (Q c^\dagger_{n,\mu} c_{m,\mu} P - P c^\dagger_{n,\mu} c_{m,\mu} Q)
\end{aligned}
$$

$$= \sum_{m,n,\mu} \sum_{i,j,\sigma} -\frac{t_{m,n}t_{i,j}}{U} [Pc_{i\sigma}^\dagger c_{j\sigma} Q c_{m,\mu}^\dagger c_{n,\mu} P + Q c_{i\sigma}^\dagger c_{j\sigma} Q c_{m,\mu}^\dagger c_{n,\mu} P -$$

$$Pc_{i\sigma}^\dagger c_{j\sigma} P c_{m,\mu}^\dagger c_{n,\mu} Q - Q c_{i\sigma}^\dagger c_{j\sigma} P c_{m,\mu}^\dagger c_{n,\mu} Q] \quad \text{(A.16)}$$

$$SH_t = \sum_{m,n,\mu} \sum_{i,j,\sigma} -\frac{t_{m,n}t_{i,j}}{U} [Q c_{i\sigma}^\dagger c_{j\sigma} P c_{m,\mu}^\dagger c_{n,\mu} P + Q c_{i\sigma}^\dagger c_{j\sigma} P c_{m,\mu}^\dagger c_{n,\mu} Q -$$

$$Pc_{i\sigma}^\dagger c_{j\sigma} Q c_{m,\mu}^\dagger c_{n,\mu} P - P c_{i\sigma}^\dagger c_{j\sigma} Q c_{m,\mu}^\dagger c_{n,\mu} Q] \quad \text{(A.17)}$$

Both $H_t S$ and SH_t contain coupling terms between the upper and lower Hubbard models, of order t^2/U. These coupling terms can be eliminated through another canonical transformation, with the correction terms having a magnitude of the order of t^3/U^2. This magnitude is low enough to justify the ignoring of these terms from this point on. Evaluation of the remaining terms $\frac{1}{2}S^2 H_U$, $\frac{1}{2}H_U S^2$, and $SH_U S$ results in

$$\frac{1}{2}S^2 H_U = \frac{1}{2}\sum_{i,j,\sigma} \frac{t_{i,j}}{U}(Qc_{i,\mu}^\dagger c_{j,\mu} P - P c_{i,\mu}^\dagger c_{j,\mu} Q) \sum_{m,n,\mu} \frac{t_{m,n}}{U}(Q c_{m,\mu}^\dagger c_{n,\mu} P - P c_{m,\mu}^\dagger c_{n,\mu} Q) \times$$

$$\sum_k U \, Q n_{k,\uparrow} n_{k,\downarrow} Q$$

$$= -\frac{1}{2}\sum_{i,j,\sigma} \sum_{m,n,\mu} \sum_k \frac{t_{i,j}t_{m,n}}{U} Q c_{i,\mu}^\dagger c_{j,\mu} P c_{m,\mu}^\dagger c_{n,\mu} Q n_{k,\uparrow} n_{k,\downarrow} Q$$

$$= -\frac{1}{2}\sum_{i,j,\sigma} \sum_{m,n,\mu} \frac{t_{i,j}t_{m,n}}{U} Q c_{i,\mu}^\dagger c_{j,\mu} P c_{m,\mu}^\dagger c_{n,\mu} Q \quad \text{(A.18)}$$

$$\frac{1}{2}H_U S^2 = -\frac{1}{2}\sum_{i,j,\sigma} \sum_{m,n,\mu} \frac{t_{i,j}t_{m,n}}{U} Q c_{i,\mu}^\dagger c_{j,\mu} P c_{m,\mu}^\dagger c_{n,\mu} Q \quad \text{(A.19)}$$

$$SH_U S = \sum_{i,j,\sigma} \frac{t_{i,j}}{U}(Q c_{i,\mu}^\dagger c_{j,\mu} P - P c_{i,\mu}^\dagger c_{j,\mu} Q) \sum_k U \, Q n_{k,\uparrow} n_{k,\downarrow} Q \times$$

$$\sum_{m,n,\mu} \frac{t_{m,n}}{U}(Q c_{m,\mu}^\dagger c_{n,\mu} P - P c_{m,\mu}^\dagger c_{n,\mu} Q)$$

$$= -\sum_{i,j,\sigma} \sum_{m,n,\mu} \sum_k \frac{t_{i,j}t_{m,n}}{U} P c_{i,\mu}^\dagger c_{j,\mu} Q n_{k,\uparrow} n_{k,\downarrow} Q c_{m,\mu}^\dagger c_{n,\mu} P$$

$$= -\sum_{i,j,\sigma} \sum_{m,n,\mu} \frac{t_{i,j}t_{m,n}}{U} P c_{i,\mu}^\dagger c_{j,\mu} Q c_{m,\mu}^\dagger c_{n,\mu} P \quad \text{(A.20)}$$

Substitution of equations A.16, A.17, A.18, A.19, and A.20 into H_2 gives

$$H_2 = -\sum_{i,j,\sigma} \sum_{m,n,\mu} \frac{t_{m,n}t_{i,j}}{U} [P c_{i,\sigma}^\dagger c_{j,\sigma} Q c_{m,\mu}^\dagger c_{n,\mu} P - Q c_{i\sigma}^\dagger c_{j\sigma} P c_{m,\mu}^\dagger c_{n,\mu} Q], \quad \text{(A.21)}$$

if all the coupling terms from equations A.16 and A.17 are disregarded. We shall also disregard the $Q c_{i,\sigma}^\dagger c_{j,\sigma} P c_{m,\mu}^\dagger c_{n,\mu} Q$ term, since it deals solely with the upper band. Let

$\sum_{i,j,\sigma} \sum_{m,n,\mu} \frac{t_{m,n} t_{i,j}}{U} P c_{i,\sigma}^\dagger c_{j,\sigma} Q c_{m,\mu}^\dagger c_{n,\mu} P = PQP$. We can write this term as

$$
\begin{aligned}
PQP &= \sum_{i,j,\sigma} \sum_{m,n,\mu} \frac{t_{m,n} t_{i,j}}{U} P c_{i,\sigma}^\dagger c_{j,\sigma} Q c_{m,\mu}^\dagger c_{n,\mu} P \\
&= \sum_{i,j,\sigma} \sum_{m,n,\mu} \frac{t_{m,n} t_{i,j}}{U} P c_{i,\sigma}^\dagger c_{j,\sigma} \delta_{j,m} n_{m,-\mu} c_{m,\mu}^\dagger c_{n,\mu} P \\
&= \sum_{i,j,\sigma} \sum_{n,\mu} \frac{t_{m,n} t_{i,j}}{U} P c_{i,\sigma}^\dagger c_{j,\sigma} c_{j,-\mu}^\dagger c_{j,-\mu} c_{j,\mu}^\dagger c_{n,\mu} P
\end{aligned}
\tag{A.22}
$$

Expressing μ as $\mu = \sigma, \mu = -\sigma$ and removing the sum over μ gives

$$
PQP = \sum_{i,j,n} \sum_\sigma \frac{t_{m,n} t_{i,j}}{U} (P c_{i,\sigma}^\dagger c_{j,\sigma} c_{j,-\sigma}^\dagger c_{j,-\sigma} c_{j,\sigma}^\dagger c_{n,\sigma} P + P c_{i,\sigma}^\dagger c_{j,\sigma} c_{j,\sigma}^\dagger c_{j,\sigma} c_{j,-\sigma}^\dagger c_{n,-\sigma} P)
\tag{A.23}
$$

The c operators obey the fermionic anticommutation rule $c_{i,\sigma} c_{j,\mu}^\dagger = \delta_{i,j} \delta_{\sigma,\mu} - c_{j,\mu}^\dagger c_{i,\sigma}$. They also obey the rule $c_{i,\sigma} c_{i,\sigma} = 0, c_{i,\sigma}^\dagger c_{i,\sigma}^\dagger = 0$, since two fermions are forbidden to have the same quantum numbers. By applying these rules to the above equation we can show that

$$
\begin{aligned}
PQP &= \sum_{i,j,n} \sum_\sigma \frac{t_{m,n} t_{i,j}}{U} (P c_{i,\sigma}^\dagger c_{j,\sigma} c_{j,\sigma}^\dagger c_{j,-\sigma}^\dagger c_{j,-\sigma} c_{n,\sigma} P + P c_{i,\sigma}^\dagger c_{j,\sigma} c_{j,-\sigma}^\dagger c_{n,-\sigma} P - \\
&\qquad P c_{i,\sigma}^\dagger c_{j,\sigma}^\dagger c_{j,\sigma} c_{j,\sigma} c_{j,-\sigma}^\dagger c_{n,-\sigma} P) \\
&= \sum_{i,j,n} \sum_\sigma \frac{t_{m,n} t_{i,j}}{U} (P c_{i,\sigma}^\dagger c_{j,-\sigma}^\dagger c_{j,-\sigma} c_{n,\sigma} P - P c_{i,\sigma}^\dagger c_{j,\sigma}^\dagger c_{j,\sigma} c_{j,-\sigma}^\dagger c_{j,-\sigma} c_{n,\sigma} P + \\
&\qquad P c_{i,\sigma}^\dagger c_{j,\sigma} c_{j,-\sigma}^\dagger c_{n,-\sigma} P)
\end{aligned}
\tag{A.24}
$$

The middle term contains $n_{j,\sigma} n_{j,-\sigma}$, making this term non-zero only if the site j is doubly occupied. However, this term also contains a P operator, which will be non-zero only if there are no doubly occupied sites. This term is then zero. Therefore we can write H_2 as

$$
H_2 = -\sum_{i,j,n} \sum_\sigma \frac{t_{j,n} t_{i,j}}{U} P(c_{i,\sigma}^\dagger c_{n,\sigma} c_{j,-\sigma}^\dagger c_{j,-\sigma} - c_{i,\sigma}^\dagger c_{n,-\sigma} c_{j,-\sigma}^\dagger c_{j,\sigma}) P
\tag{A.25}
$$

For the case when $i = n$, this becomes

$$
H_2 = \sum_{i,j} \sum_\sigma \frac{(t_{i,j})^2}{U} P(c_{i,\sigma}^\dagger c_{i,-\sigma} c_{j,-\sigma}^\dagger c_{j,\sigma} - c_{i,\sigma}^\dagger c_{i,\sigma} c_{j,-\sigma}^\dagger c_{j,-\sigma}) P
\tag{A.26}
$$

This can be expressed in terms of the spin operator S. If one evaluates the product

$\vec{S}_i \cdot \vec{S}_j$, we can arrive at

$$\vec{S}_i \cdot \vec{S}_j = \frac{1}{2} \sum_\sigma (c_{i,\sigma}^\dagger c_{i,-\sigma} c_{j,-\sigma}^\dagger c_{j,\sigma} - c_{i,\sigma}^\dagger c_{i,\sigma} c_{j,-\sigma}^\dagger c_{j,-\sigma}) + \frac{n_i n_j}{4}. \qquad (A.27)$$

If we substitute this expression into equation A.26, and restrict the sum over i and j to be over bonds as opposed to sites to eliminate double counting, then H_2 becomes

$$H_2 = \sum_{<i,j>} \frac{4t_{i,j}^2}{U} P(S_i \cdot S_j - \frac{n_i n_j}{4}) P. \qquad (A.28)$$

Now let $\tilde{H} = \tilde{H}_{PP} + \tilde{H}_{QQ}$, where $\tilde{H}_{PP}$ only includes interactions between the lower Hubbard band states, and $\tilde{H}_{QQ}$ only includes interactions between the upper Hubbard band states. We can write $\tilde{H}_{PP}$ as

$$\tilde{H}_{PP} = -\sum_{i,j,\sigma} t_{i,j} P c_{i,\sigma}^\dagger c_{j,\sigma} P + \sum_{<i,j>} J_{i,j} P(S_i \cdot S_j - \frac{n_i n_j}{4}) P, \qquad (A.29)$$

where $J_{i,j} = 4t_{i,j}^2/U$. This is the $t-J$ model Hamiltonian, to second order in t. Not included are the higher order terms of order t^3/U^2. Also note that this Hamiltonian does not include the cases of equation A.25 where $i \neq n$. These terms are three-site spin terms, the strength of which is generally indicated by the parameter t_s. This parameter is of the same order as J, but has generally been excluded from most studies of the $t-J$ model.